

## COZMIC. III. Cosmological Zoom-in Simulations of SIDM with Suppressed Initial Conditions

ETHAN O. NADLER,<sup>1,2,3</sup> RUI AN,<sup>2</sup> DANENG YANG,<sup>4,5</sup> HAI-BO YU,<sup>5</sup> ANDREW BENSON,<sup>1</sup> AND VERA GLUSCEVIC<sup>2</sup>

<sup>1</sup>*Carnegie Observatories, 813 Santa Barbara Street, Pasadena, CA 91101, USA*

<sup>2</sup>*Department of Physics & Astronomy, University of Southern California, Los Angeles, CA 90007, USA*

<sup>3</sup>*Department of Astronomy & Astrophysics, University of California, San Diego, La Jolla, CA 92093, USA*

<sup>4</sup>*Purple Mountain Observatory, Chinese Academy of Sciences, Nanjing 210023, China*

<sup>5</sup>*Department of Physics and Astronomy, University of California, Riverside, CA 92521, USA*

### ABSTRACT

We present eight cosmological dark matter (DM)–only zoom-in simulations of a Milky Way-like system that include suppression of the linear matter power spectrum  $P(k)$ , and/or velocity-dependent DM self-interactions, as the third installment of the COZMIC suite. We consider a model featuring a massive dark photon that mediates DM self-interactions and decays into massless dark fermions. The dark photon and dark fermions suppress linear matter perturbations, resulting in dark acoustic oscillations in  $P(k)$ , which ultimately affect dwarf galaxy scales. The model also features a velocity-dependent elastic self-interaction between DM particles (SIDM), with a cross section that can alleviate small-scale structure anomalies. For the first time, our simulations test the impact of  $P(k)$  suppression on gravothermal evolution in an SIDM scenario that leads to core collapse in (sub)halos with present-day virial masses below  $\approx 10^9 M_\odot$ . In simulations with  $P(k)$  suppression and self-interactions, the lack of low-mass (sub)halos and the delayed growth of structure reduce the fraction of core-collapsed systems relative to SIDM simulations without  $P(k)$  suppression. In particular,  $P(k)$  suppression that saturates current warm DM constraints almost entirely erases core collapse in isolated halos. Models with less extreme  $P(k)$  suppression produce core collapse in  $\approx 20\%$  of subhalos and  $\approx 5\%$  of isolated halos above  $10^8 M_\odot$ , and also increase the abundance of extremely low-concentration isolated low-mass halos relative to SIDM. These results reveal a complex interplay between early and late-universe DM physics, revealing new discovery scenarios in the context of upcoming small-scale structure measurements.

*Keywords:* Dark matter (353);  $N$ -body simulations (1083); Galaxy dark matter halos (1880)

### 1. INTRODUCTION

Small-scale cosmic structure is a key probe of dark matter (DM) physics, including its interactions (e.g., see Buckley & Peter 2018 and Gluscevic et al. 2019 for reviews). Different kinds of DM physics beyond gravity—i.e., beyond the cold, collisionless DM (CDM) paradigm—are often parameterized and modeled separately. For example, free-streaming of warm DM particles (WDM; Bond & Szalay 1983; Bode et al. 2001) imprints a small-scale cutoff in the linear matter power spectrum  $P(k)$ , which reduces low-mass halo and subhalo abundances relative to CDM. Meanwhile, interactions within the dark sector, captured by self-interacting DM models (SIDM; Spergel & Steinhardt 2000), affect (sub)halos’ internal structure, including their density profiles and shapes. These signatures are often intertwined; for example, SIDM can suppress subhalo abundances through subhalo–host halo interactions and enhanced stripping of cored halos (e.g., Vogelsberger et al. 2012; Nadler et al. 2020a).

$P(k)$  suppression associated with WDM-like models is not typically included when modeling SIDM. However, models that feature DM interactions often affect  $P(k)$ . This is well known for DM that interacts with the Standard Model or dark radiation (e.g., Boehm et al. 2001; Boehm & Schaeffer 2005; Feng et al. 2009; van den Aarssen et al. 2012; Buckley et al. 2014). For example, Boehm et al. (2002) show that DM–Standard Model interactions can impact  $P(k)$  in a way that mimics WDM (also see Nadler et al. 2019a). On the other hand, DM self-interactions are inefficient until the high densities at the centers of virialized halos are achieved. For this reason, SIDM does not significantly alter large-scale structure observables relative to CDM (e.g., Rocha et al. 2013).

Although the direct impact of self-interactions on  $P(k)$  is minor, favored SIDM models feature a velocity-dependent cross section with a low-mass dark mediator (e.g., see Tulin & Yu 2018 and Adhikari et al. 2022 for reviews); this mediator, and other dark sector particles that accompany the self-interactions, affect the growth of linear matter perturbations and suppress  $P(k)$ . These scenarios therefore lead to WDM-like initial conditions, but also feature SIDM phenomenology at late times; thus we refer to them as WSIDM.

As a benchmark example of WSIDM, we consider a model with an 0.1 GeV DM particle and a  $\sim 10$  keV dark photon that mediates DM self-interactions (Huo et al. 2018). The mediator couples to a dark fermion, which increases the effective number of relativistic species at early times. We will show that (sub)halo abundances and density profiles are sensitive to both  $P(k)$  suppression *and* self-interactions. Crucially, our WSIDM scenario features a velocity-dependent SIDM cross section that can alleviate small-scale structure anomalies by producing core-collapse in low-mass (sub)halos (Balberg et al. 2002; Koda & Shapiro 2011; Essig et al. 2019). Furthermore, it produces  $P(k)$  cutoffs tested by current small-scale structure data, allowing us to assess detectability of WSIDM with upcoming data.

We note that the same combination of effects arises in the Effective Theory of Structure Formation framework (ETHOS; Cyr-Racine et al. 2016; Vogelsberger et al. 2016). However, as we will demonstrate,  $P(k)$  suppression is so strong in Vogelsberger et al. (2016) that core collapse is not achieved. Thus, to date, no WSIDM simulations have been performed which include  $P(k)$  suppression and capture the full range of (sub)halos’ gravothermal evolution. It is critical to understand the interplay between these effects.

Here, we perform the first WSIDM simulations that capture core collapse. The SIDM cross section we consider (hereafter “MilkyWaySIDM”) was originally presented in Yang et al. (2023) and is shown in the left panel of Figure 1. This model is similar to those considered in Correa (2021) and Turner et al. (2021), and is motivated as follows. At large velocities,  $v \approx 1000$  km s<sup>-1</sup>, observations of galaxy clusters and large elliptical galaxies place stringent upper limits on the SIDM cross section of  $\approx 0.1$  to 1 cm<sup>2</sup> g<sup>-1</sup> (Kaplinghat et al. 2016; Sagunski et al. 2021; Andrade et al. 2022; Kong et al. 2024). Constraints are weaker at lower velocities, corresponding to galaxy group and Milky Way (MW)-scales. At dwarf galaxy scales ( $v \approx 10$  km s<sup>-1</sup>) data rule out a velocity-independent cross section above  $\approx 5$  cm<sup>2</sup> g<sup>-1</sup> (e.g., Correa 2021; Silverman et al. 2023). In particular, a velocity-independent cross section on dwarf scales predicts uniformly cored subhalos, which are challenging to reconcile with MW satellites’ observed inner densities and bright dwarfs’ diverse rotation curves (e.g., Valli & Yu 2018; Read et al. 2018; Zavala et al. 2019; Kim & Peter 2021; Silverman et al. 2023; Yang et al. 2023). This challenge is compounded by the orbital properties of observed satellites (e.g., Kaplinghat et al. 2019; Sameie et al. 2020; Slone et al. 2023).

On the other hand, the MilkyWaySIDM cross section predicts diverse (sub)halo density profiles due to core formation and collapse. Strong, velocity-dependent SIDM models can explain observations of very low-concentration ultra-diffuse galaxies (e.g., Kong et al. 2022; Zhang et al. 2024a), extremely concentrated strong-lensing substructure detected by gravitational imaging (Minor et al. 2021a; Yang & Yu 2021; Nadler et al. 2023a; Zeng et al. 2023), and the properties of the GD-1 stellar stream perturber (Zhang et al. 2024b). These scenarios can also be constrained with strong lensing flux ratio statistics (Gilman et al. 2021, 2023; Tran et al. 2024).

Previous studies that simulated the MilkyWaySIDM cross section or similar models all assumed CDM initial conditions (ICs), with the exception of Vogelsberger et al. (2016). The characteristic suppression scale in  $P(k)$  is determined by the kinetic decoupling temperature of the dark fermion–DM interaction,  $T_{\text{kd}}$ . In our scenario,  $T_{\text{kd}}$  is controlled by the DM self-coupling, mediator mass, and dark fermion temperature (Huo et al. 2018). We will show that natural values for these parameters yield a  $P(k)$  cutoff on dwarf galaxy scales, thereby affecting the formation and evolution of the *same* (sub)halos that are impacted by self-interactions. In particular, we consider three  $P(k)$  cutoffs that are constrained by current observations of the Lyman- $\alpha$  forest (Viel et al. 2013; Iršič et al. 2017, 2024), MW satellites (Nadler et al. 2021b), and strong gravitational lensing (Nadler et al. 2021a). The corresponding transfer functions set the ICs for our simulations and are shown in the right panel of Figure 1.

With these ingredients, we run eight new high-resolution cosmological DM-only zoom-in simulations of a MW analog from the Milky Way-est suite (Buch et al. 2024), in WSIDM models.<sup>1</sup> Our simulations are part of the COsmological ZooM-in simulations with Initial Conditions beyond CDM (COZMIC) suite, which includes over 100 beyond-CDM simulations with ICs for warm, fuzzy, and baryon-scattering DM (Nadler et al. 2024a, hereafter Paper I), and for models with a fractional non-CDM component (Paper II; An et al. 2024). We show that the severity of  $P(k)$  suppression influences whether SIDM core collapse occurs or not. Thus, WSIDM can change predictions for SIDM (sub)halo profiles and simultaneously affect (sub)halo abundances. Combining upcoming observations of strong gravitational lenses, to probe (sub)halo density profiles (Minor et al. 2021b; Despali et al. 2024), and the MW satellite population, to probe the subhalo mass function (SHMF; Nadler et al. 2024b), will therefore test WSIDM.

This paper is organized as follows. In Section 2, we describe our WSIDM model and how it maps to both  $P(k)$  and the SIDM cross section. In Section 3, we describe our method for generating WSIDM ICs and performing zoom-in simulations that include both suppressed ICs and self-interactions. In Section 4, we present our results, focusing on (S)HMFs and structural properties. In Section 5, we study how  $P(k)$  suppression and gravothermal evolution interplay using matched (sub)halos from our simulations; we make predictions for dwarf galaxy density profiles in Section 6. We discuss our results in Section 7 and conclude in Section 8.

We adopt the following cosmological parameters:  $h = 0.7$ ,  $\Omega_{\text{m}} = 0.286$ ,  $\Omega_{\text{b}} = 0.049$ ,  $\Omega_{\Lambda} = 0.714$ ,  $\sigma_8 = 0.82$ , and  $n_s = 0.96$  (Paper I; Hinshaw et al. 2013). Halo masses are defined via the Bryan & Norman (1998) virial overdensity, which corresponds to  $\Delta_{\text{vir}} \approx 99 \times \rho_{\text{crit}}$  in our cosmology, where  $\rho_{\text{crit}}$  is the critical density of the Universe at  $z = 0$ . We refer to halos within the virial radius of our MW host as “subhalos,” and

<sup>1</sup> We use “SIDM” for models with *only* self-interactions and no  $P(k)$  suppression, i.e., SIDM that is cold on all scales relevant for our simulations.

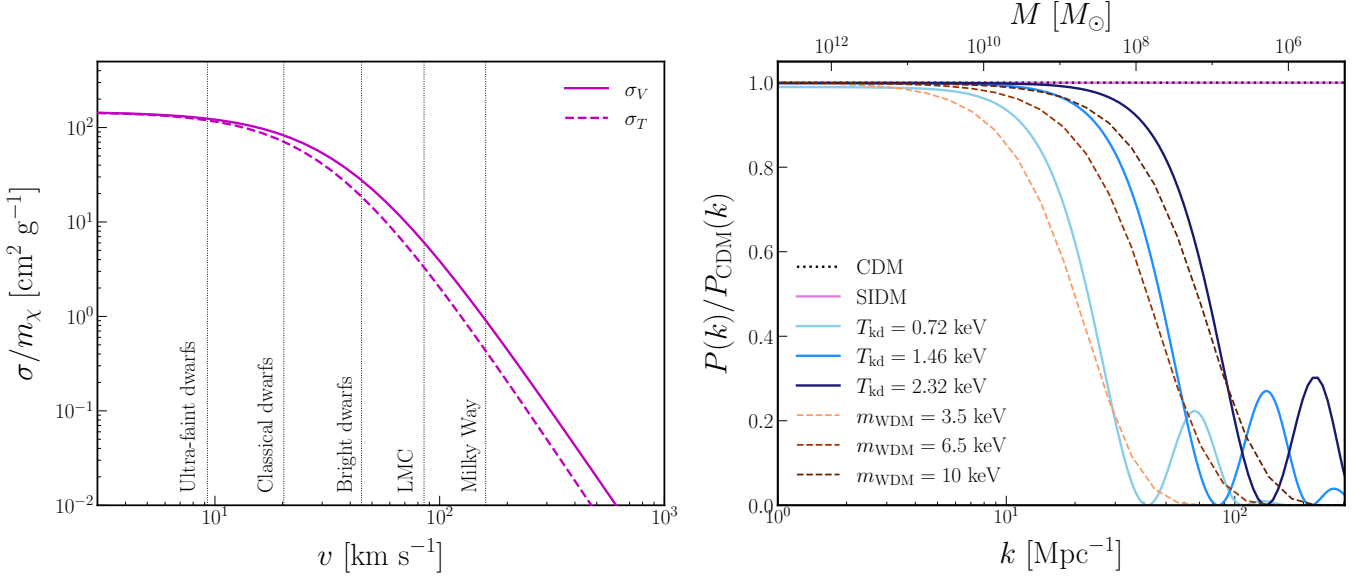


**Figure 1.** *Left panel:* Viscosity (solid) and momentum-transfer (dashed) self-interaction cross sections, which define our MilkyWaySIDM model (Yang et al. 2023). Note that our SIDM implementation captures the velocity and angular dependence of the differential cross section (see Section 3.2). Vertical dotted lines show maximum circular velocities of our MW-like host ( $M_{\text{vir}} = 10^{12} M_{\odot}$ ), LMC analog ( $M_{\text{vir}} = 10^{11} M_{\odot}$ ), and halos expected to host bright ( $M_{\text{vir}} = 10^{10} M_{\odot}$ ), classical ( $M_{\text{vir}} = 10^9 M_{\odot}$ ), and ultra-faint ( $M_{\text{vir}} = 10^8 M_{\odot}$ ) dwarf galaxies. *Right panel:* Ratio of the linear matter power spectrum for each model we simulate (colored lines) relative to CDM (horizontal dotted black line). Our SIDM simulation (magenta) uses CDM initial conditions. We simulate  $T_{\text{kd}} = 0.72, 1.46,$  and  $2.32$  keV (lightest to darkest blue) with and without self-interactions; we simulate WDM models with  $m_{\text{WDM}} = 3.5, 6.5,$  and  $10$  keV without self-interactions (lightest to darkest red). Top ticks show halo masses calculated in linear theory (Nadler et al. 2019a; Paper I). The largest scale shown roughly corresponds to the size of our zoom-in regions, and the smallest to the Nyquist frequency of the high-resolution simulations used for our main analyses.

halos outside the virial radius of any larger halo as “isolated halos.” We work in natural units with  $c = \hbar = 1$ .

## 2. WSIDM MODEL

We consider the interaction Lagrangian (Huo et al. 2018)

$$\mathcal{L}_{\text{int}} = -ig_{\chi}\bar{\chi}\gamma^{\mu}\chi\phi_{\mu} + m_{\chi}\bar{\chi}\chi + \frac{1}{2}m_{\phi}^2\phi^{\mu}\phi_{\mu} - ig_f\bar{f}\gamma^{\mu}f\phi_{\mu}, \quad (1)$$

which contains an SIDM particle  $\chi$  with mass  $m_{\chi}$ , a massless dark fermion  $f$ , and an SIDM mediator  $\phi$  with mass  $m_{\phi}$ . The coupling constants  $g_{\chi}$  ( $g_f$ ) determine the strength of DM self-interactions (dark fermion–mediator interactions); we follow Huo et al. (2018) and set  $g_{\chi} = g_f$ . Finally,  $\xi$  parameterizes the ratio of dark-to-visible sector temperature (Feng et al. 2008). In this scenario, the DM relic abundance is determined by annihilation of  $\chi$  to  $\phi$  in the early Universe. Matching  $\Omega_{\text{m}}$  to the DM relic density thus imposes a relation between  $g_{\chi}$  and  $m_{\chi}$ . Here, we fix  $m_{\chi} = 0.1$  GeV, which determines both  $g_{\chi}$  and  $m_{\phi}$  based on the desired SIDM cross section, as described below. We therefore remain agnostic about the details of the underlying DM production mechanism.

Meanwhile, the dark fermion contributes to the effective number of relativistic degrees of freedom in the early Universe,  $N_{\text{eff}}$ , with  $N_{\text{eff}} = 3.046 + \Delta N_{\text{eff}} = 3.046 + (11/4)^{4/3}\xi^4$ . With  $m_{\chi}$  fixed and  $g_{\chi}$  and  $m_{\phi}$  chosen to yield our desired SIDM cross section,  $\xi$  is the only remaining parameter that

determines the cutoff scale in  $P(k)$ . Below, we derive three values of  $\xi$  that produce desired  $P(k)$  cutoff scales; all of these are consistent with bounds from Planck on  $\Delta N_{\text{eff}}$ , which imply  $\xi \lesssim 0.5$  (Archidiacono et al. 2017). Thus, our model yields a DM relic abundance and expansion history consistent with observations while producing a specific SIDM cross section and desired  $P(k)$  cutoffs.

Specifically, to derive  $g_{\chi}$  and  $m_{\phi}$ , we write the differential SIDM cross section as (Yang & Yu 2022)

$$\frac{d\sigma}{d\cos\theta} = \frac{\sigma_0 w^4}{2[w^2 + v^2 \sin^2(\theta/2)]^2}, \quad (2)$$

where  $\sigma_0 \equiv g_{\chi}^4/(4\pi m_{\chi}^2 w^4)$  is the cross section amplitude,  $w \equiv m_{\phi}/m_{\chi}$ ,  $v$  is the relative velocity of SIDM particles, and  $\theta$  is their scattering angle. We use the MilkyWaySIDM model from Yang et al. (2023), which is similar to the models proposed in Correa (2021) and Turner et al. (2021). In particular, we set  $\sigma_0 = 147.1 \text{ cm}^2 \text{ g}^{-1}$  and  $w = 24.33 \text{ km s}^{-1}$ , which yields  $g_{\chi} = 7.8 \times 10^{-4}$  and  $m_{\phi} = 8.11 \text{ keV}$  given  $m_{\chi} = 0.1 \text{ GeV}$ . Note that  $g_{\chi}^2/w \ll 1$ , so the Born approximation for  $d\sigma/d\cos\theta$  is valid (Feng et al. 2010; Tulin et al. 2013). The left panel of Figure 1 shows the momentum transfer and viscosity cross sections, calculated following Yang & Yu (2022), Yang et al. (2023), and Nadler et al. (2023a). Note that the viscosity cross section effectively captures the full, angularly dependent SIDM scattering (Yang & Yu 2022).

The impact of this WSIDM model on  $P(k)$  is parameterized by the temperature of the visible sector  $T_{\text{kd}}$  when DM kinetically decouples with the dark fermion, given by (Huo et al. 2018)

$$T_{\text{kd}} = \frac{1.4 \text{ keV}}{\sqrt{g_\chi g_f}} \left( \frac{m_\chi}{100 \text{ GeV}} \right)^{\frac{1}{4}} \left( \frac{m_\phi}{10 \text{ MeV}} \right) \left( \frac{g_*}{3.38} \right)^{\frac{1}{8}} \left( \frac{\xi}{0.5} \right)^{-\frac{3}{2}}$$

$$= 0.26 \text{ keV} \times \left( \frac{\xi}{0.5} \right)^{-\frac{3}{2}}, \quad (3)$$

where  $g_*$  is the number of relativistic degrees of freedom at the redshift of decoupling, which we always set to 3.38, as kinetic decoupling occurs after electron–positron annihilation in all models we consider. We choose values of  $\xi$  such that the resulting half-mode wave number  $k_{\text{hm}}$ , defined by  $P(k_{\text{hm}})/P_{\text{CDM}}(k_{\text{hm}}) \equiv 0.25$  and returned by our  $P(k)$  calculations in Section 3.1, matches three benchmark models of thermal-relic WDM:  $m_{\text{WDM}} = 3.5, 6.5,$  and  $10 \text{ keV}$ . This yields  $T_{\text{kd}} = 0.72, 1.46,$  and  $2.32 \text{ keV}$ , respectively. These correspond to  $\xi = 0.25, 0.15,$  and  $0.11$ , all of which are consistent with the Planck constraint mentioned above.

The right panel of Figure 1 shows linear matter power spectra normalized to CDM for these scenarios, calculated using CLASS. The cutoff scales are respectively chosen to saturate current WDM limits from the Lyman- $\alpha$  forest (Viel et al. 2013; Iršič et al. 2017, 2024), the MW satellite population (Nadler et al. 2021b), and a combination of MW satellites and strong gravitational lensing flux ratio statistics (Nadler et al. 2021a). The  $10 \text{ keV}$  case is also comparable to the WDM sensitivity of upcoming dwarf galaxy surveys (Nadler et al. 2024b). Our most suppressed scenario,  $T_{\text{kd}} = 0.72 \text{ keV}$ , is slightly colder than the ETHOS-2 ( $T_{\text{kd}} = 0.33 \text{ keV}$ ) and ETHOS-3 ( $T_{\text{kd}} = 0.51 \text{ keV}$ ) models from Vogelsberger et al. (2016) and Sameie et al. (2019). The other models have cutoffs on smaller scales and are less suppressed than the  $T_{\text{kd}} = 1 \text{ keV}$  model studied in Huo et al. (2018).

### 3. SIMULATIONS

We now describe our procedure for generating ICs (Section 3.1) and running our zoom-in simulations (Section 3.2).

#### 3.1. Initial Conditions

To generate transfer functions for our WSIDM zoom-in simulations, we run a modified version of CAMB (Lewis & Bridle 2002) developed by Cyr-Racine et al. (2016). We also generate transfer functions for the benchmark WDM models discussed above using CLASS (Lesgourgues 2011; see Paper I for details). The right panel of Figure 1 compares all of the transfer functions we simulate. In addition to the initial cutoff in  $P(k)$ , our  $T_{\text{kd}}$  models feature dark acoustic oscillations (DAOs) on very small scales. Based on the results from Paper I, we do not expect these low-amplitude DAOs to significantly alter (sub)halo abundances compared to the half-mode matched WDM models; we confirm and quantify this statement in Section 4.2 and Appendix B.

Following Paper I, we input these transfer functions to MUSIC (Hahn & Abel 2011) to generate ICs for one of

the MW-like hosts from Paper I, Halo004; CDM ICs were originally drawn from the Milky Way-est suite (Buch et al. 2024). This host has a  $z = 0$  virial mass of  $1.03 \times 10^{12} M_\odot$ , contains a subhalo analogous to the LMC that accreted recently, with a peak virial mass of  $1.74 \times 10^{11} M_\odot$ , and merges with an analog of Gaia–Sausage–Enceladus at  $z = 1.4$  (Buch et al. 2024; Paper I). For our main analyses, we focus on “high-resolution” simulations initialized at  $z = 99$  using five refinement regions, with a DM particle mass of  $m_{\text{part}} = 5.0 \times 10^4 M_\odot$  and Plummer-equivalent gravitational softening of  $\epsilon = 80 \text{ pc } h^{-1}$  in the highest-resolution region. In Appendix A, we simulate the same models with one fewer refinement region to assess convergence.

#### 3.2. Zoom-in Simulations

We run COZMIC III simulations using a version of GADGET-2 (Springel 2005) modified to include SIDM, with other code settings identical to Paper I. We use the SIDM implementation from Yang et al. (2023), with elastic self-interactions modeled as described in Yang & Yu (2022). This implementation captures the full velocity and angular dependence of the differential SIDM scattering cross section (Equation 2). We generate halo catalogs and merger trees using ROCKSTAR and CONSISTENT-TREES (Behroozi et al. 2013a,b), and we analyze all simulations at  $z = 0$ . In each simulation, we analyze all subhalos within the virial radius of the MW host and all isolated halos within 3 Mpc of the MW center, following Yang et al. (2023); the fraction of low-resolution particles within this volume is negligible.

We simulate CDM, the three WDM models shown in the right panel of Figure 1, the three  $T_{\text{kd}}$  models shown in the same panel without self-interactions (hereafter “ $T_{\text{kd}}$ -only” simulations), the same three  $T_{\text{kd}}$  models with self-interactions (hereafter “WSIDM” simulations), and CDM ICs with our self-interaction model (hereafter our “SIDM” simulation). We have resimulated all cases at lower resolution (i.e., with one fewer refinement level) and present a convergence test in Appendix A. Note that our CDM,  $m_{\text{WDM}} = 6.5 \text{ keV}$ , and  $m_{\text{WDM}} = 10 \text{ keV}$  simulations are the same as those presented in Paper I; our SIDM,  $m_{\text{WDM}} = 3.5 \text{ keV}$  and  $T_{\text{kd}}$ -only and WSIDM simulations are new. Thus, we present a total of eight new high-resolution simulations in this work. Our analysis is mainly based on the CDM, SIDM,  $T_{\text{kd}}$ -only, and WSIDM simulations; we use the WDM simulations to isolate the effects of  $P(k)$  suppression and test the impact of WSIDM DAOs in Appendix B. We leave a detailed comparison between our WDM and other simulations to future work.

#### 3.3. Analysis Procedures

We restrict our (sub)halo abundance measurements to objects with more than 300 particles at  $z = 0$ , i.e., with present-day virial masses  $M_{\text{vir}} > 1.5 \times 10^7 M_\odot$  (Nadler et al. 2023b). When analyzing (sub)halo structural properties and density profiles, we only consider objects with more than 2000 particles at  $z = 0$ , or  $M_{\text{vir}} > 10^8 M_\odot$ , following Yang et al. (2023). This roughly selects (sub)halos with present-day maximum circular velocities  $V_{\text{max}} \gtrsim 7 \text{ km s}^{-1}$ ; we define  $R_{\text{max}}$  as the ra-

**Table 1.** Summary of COZMIC III Simulations

Model	$f_{\text{iso},7}$	$f_{\text{iso},8}$	$f_{\text{sub},7}$	$f_{\text{sub},8}$	$f_{\text{cc,iso},8}$	$f_{\text{cc,sub},8}$	Color and Linestyle
CDM	1.0	1.0	1.0	1.0	–	–	.....
SIDM	0.98	0.99	0.83	0.97	0.13	0.19	—
$m_{\text{WDM}} = 3.5$ keV	0.16	0.42	0.22	0.49	–	–	- - - - -
$m_{\text{WDM}} = 6.5$ keV	0.46	0.81	0.50	0.81	–	–	- - - - -
$m_{\text{WDM}} = 10$ keV	0.73	0.93	0.76	0.98	–	–	- - - - -
$T_{\text{kd}} = 0.72$ keV	0.30	0.51	0.30	0.48	–	–	- - - - -
$T_{\text{kd}} = 1.46$ keV	0.56	0.85	0.61	0.92	–	–	- - - - -
$T_{\text{kd}} = 2.32$ keV	0.78	0.97	0.82	0.99	–	–	- - - - -
$T_{\text{kd}} = 0.72$ keV + SIDM	0.30	0.51	0.25	0.46	0.02	0.02	—
$T_{\text{kd}} = 1.46$ keV + SIDM	0.55	0.84	0.49	0.89	0.02	0.08	—
$T_{\text{kd}} = 2.32$ keV + SIDM	0.77	0.96	0.72	0.96	0.04	0.17	—

NOTE—The first column lists the DM model. The second column lists the fraction of isolated halos with  $M_{\text{vir}} > 1.5 \times 10^7 M_{\odot}$  ( $M_{\text{vir}} > 10^8 M_{\odot}$ ) relative to CDM, denoted  $f_{\text{iso},7}$  ( $f_{\text{iso},8}$ ). Isolated halos must reside within 3 Mpc of the host center and cannot be within the virial radius of any large halo. The third column lists the fraction of our MW host’s subhalos above the same mass cuts, denoted  $f_{\text{sub},7}$  ( $f_{\text{sub},8}$ ). The fourth (fifth) column lists the fraction of core-collapsed isolated halos (subhalos) with  $M_{\text{vir}} > 10^8 M_{\odot}$ , denoted  $f_{\text{cc,iso},8}$  ( $f_{\text{cc,sub},8}$ ). The core-collapsed fraction is determined using the parametric SIDM model from Yang et al. (2024b,a); see Section 3.3. Note that there are 583 (100) subhalos and 3872 (759) isolated halos with  $M_{\text{vir}} > 1.5 \times 10^7 M_{\odot}$  ( $M_{\text{vir}} > 10^8 M_{\odot}$ ) in our CDM simulation.

dius within each subhalo at which  $V_{\text{max}}$  is achieved. Based on Paper I, spurious (sub)halos formed through artificial fragmentation contribute negligibly to our WSIDM (sub)halo populations above the present-day mass resolution limit.

Throughout, we use “peak” to denote the largest value of a quantity achieved along a given (sub)halo’s main branch, e.g.,  $M_{\text{peak}}$  is the largest value that a (sub)halo’s most massive progenitor achieves at any snapshot. Following Paper I, we measure (S)HMFs using  $M_{\text{peak}}$  because it more closely relates to the comoving wave number that sources halos of a given mass than present-day (stripped) mass, and is thus easier to interpret, particularly for subhalos. Because  $M_{\text{peak}}$  functions converge slowly in the absence of a present-day mass cut (e.g., Nadler et al. 2023b; Mansfield et al. 2024), we always apply the  $M_{\text{vir}}(z=0)$  cuts described above before measuring (S)HMFs. Note that the WDM SHMF suppression models we compare to, from Paper I, were derived using a similar set of cuts.

To model SIDM (sub)halos’ gravothermal evolution, we apply the parametric model from Yang et al. (2024b,a) to our simulations. This model analytically predicts SIDM density profile evolution based on CDM  $V_{\text{max}}$  and  $R_{\text{max}}$  histories. Gravothermal evolution is parameterized by  $\tau \equiv t/t_c$ , where  $t$  is the time since a (sub)halo formed and  $t_c$  is the core-collapse timescale (e.g., Essig et al. 2019). Specifically, we calculate

$$\tau_0 = \int_{t_f}^{t_0} \frac{dt}{t_c(t)}, \quad (4)$$

where  $t_0 = 13.6$  Gyr is the age of the universe today, and  $t_f$  is computed for each (sub)halo using a universal halo mass-formation time relation; see Yang et al. 2024b for details.

We apply the model to our CDM simulation in order to predict SIDM (sub)halos’  $\tau_0$  values, and to each of our  $T_{\text{kd}}$ -only simulations to predict WSIDM (sub)halos’  $\tau_0$  values. As a result, only (sub)halos that are matched between our CDM and SIDM or our  $T_{\text{kd}}$ -only and WSIDM simulations are used. We discard a handful of (sub)halos with noisy  $V_{\text{max}}$  and  $R_{\text{max}}$  histories that lead to undefined  $\tau_0$  values, and clip the predicted  $\tau_0$  values to a maximum of 1.1, since the parametric model has been validated against SIDM simulations up to this point (Yang et al. 2024a). We define  $\tau_0 < 0.15$  as the core-forming regime, since  $\tau_0 = 0.15$  corresponds to the time when the lowest central density and maximum core size is achieved, and  $\tau_0 > 0.75$  as the core-collapsed regime, since systems are rapidly collapsing at this point and have central densities that exceed corresponding (sub)halos with no self-interactions (e.g., see Roberts et al. 2024).

The parametric model accurately predicts (sub)halo  $V_{\text{max}}$ ,  $R_{\text{max}}$ , and density profile evolution histories, with an  $\approx 10\%$  to 50% accuracy for (sub)halo density profiles when applied to cosmological CDM simulations and compared to corresponding SIDM simulations (Yang et al. 2024a). We find that the parametric model’s accuracy is qualitatively similar when applied to our simulations with only  $P(k)$  suppression and compared to our WSIDM simulation results. Thus, we use the parametric model to compare the  $\tau_0$  distribution and fraction of core-collapsed halos between our SIDM and WSIDM

models. We leave detailed testing of the parametric model using WSIDM simulations for future work.

#### 4. RESULTS

We now present our simulation results, focusing on host halo properties (Section 4.1), halo and subhalo mass function suppression relative to CDM (Section 4.2) and structural properties, as encoded in the  $R_{\max}$ - $V_{\max}$  relation (Section 4.3) and core-collapsed fraction (Section 4.4). Key results from the full set of high-resolution simulations are summarized in Table 1, and the  $z = 0$  snapshots of the CDM, SIDM,  $T_{\text{kd}} = 0.72$  keV-only, and  $T_{\text{kd}} = 0.72$  keV WSIDM simulations are visualized in Figure 2.

##### 4.1. Host Halo Properties

The MW-like host’s mass accretion history is nearly identical to CDM in our simulations with self-interactions and/or  $P(k)$  suppression, consistent with the results of Papers I and II for models that suppress  $P(k)$ . The SIDM and WSIDM simulations feature an  $\mathcal{O}(\text{kpc})$  core in the host’s density profile, regardless of  $T_{\text{kd}}$ ; we present the corresponding host density profiles in Appendix E. Note that the  $P(k)$  suppression is negligible on the scale of the MW host and LMC analog, for all models we simulate (see the right panel of Figure 1).

##### 4.2. Mass Functions

In SIDM scenarios without small-scale  $P(k)$  suppression, the isolated halo mass function is not significantly suppressed relative to CDM, while the subhalo mass function is only suppressed if the cross section is large at the subhalo infall velocity scale ( $\approx 100 \text{ km s}^{-1}$ , for MW subhalos; Nadler et al. 2020a). Thus, it is often sufficient to model SIDM effects on (sub)halo density profiles alone, without considering mass functions. Indeed, (semi-)analytic models often use CDM merger trees as a template for modeling SIDM physics (e.g., Yang et al. 2024b,a). However, in WSIDM,  $P(k)$  suppression can significantly alter underlying (sub)halo abundances.

To demonstrate this, Figure 3 compares the isolated-halo (left) and subhalo (right) cumulative peak-mass functions. We find that SIDM alone does not affect isolated halo abundances, consistent with the result from Yang et al. (2023). A  $P(k)$  cutoff suppresses the isolated halo abundances, and the magnitude of this suppression is not affected by the presence of self-interactions (compare the solid and dashed blue lines in the left panel of Figure 3); thus, isolated-halo abundances are solely determined by  $P(k)$ . Specifically, comparing WSIDM simulations with  $T_{\text{kd}} = 0.72, 1.46,$  and  $2.32$  keV, to their CDM counterparts, we respectively find that 30%, 55%, and 77% of isolated halos with  $M_{\text{vir}} > 1.5 \times 10^7 M_{\odot}$  are still present; these differences are significant and larger than the statistical uncertainty on the CDM mass function.

The right panel of Figure 3 shows that the cumulative SHMF is suppressed by  $\approx 20\%$  down to  $M_{\text{vir}} = 1.5 \times 10^7 M_{\odot}$  in the SIDM simulation, consistent with Yang et al. (2023); also see Turner et al. (2021) and Lovell & Zavala (2023). This suppression is due to a combination of SIDM evaporation from subhalo–host halo interactions and enhanced tidal

disruption of subhalos featuring cored (rather than cuspy) profiles (e.g., Vogelsberger et al. 2012; Nadler et al. 2020a). Introducing a  $P(k)$  cutoff within WSIDM simulations further enhances the suppression: only 25%, 49%, and 72% of subhalos with  $M_{\text{vir}} > 1.5 \times 10^7 M_{\odot}$  remain, relative to CDM, in the  $T_{\text{kd}} = 0.72, 1.46,$  and  $2.32$  keV cases, respectively; again, these differences are significant, given the statistical uncertainty on the CDM SHMF. Compared to our simulations with  $P(k)$  suppression alone, WSIDM SHMFs are slightly more suppressed, at the  $\approx 5\%$  level (compare the solid and dashed lines in the bottom-right panel of Figure 3). Thus, SHMF suppression is mainly determined by the  $P(k)$  cutoff, rather than late-time self-interactions, for the models we simulate.

Our  $T_{\text{kd}} = 0.72$  keV WSIDM SHMF suppression is weaker than the simulation predictions for ETHOS-2 and ETHOS-3 models in Vogelsberger et al. (2016), which included  $P(k)$  suppression and an SIDM cross section comparable to our WSIDM models. This is consistent with the slightly stronger  $P(k)$  suppression in ETHOS-2 and ETHOS-3 models compared to our  $T_{\text{kd}} = 0.72$  keV case. In Section 5, we will demonstrate that core-collapse is almost entirely avoided in models with such extreme  $P(k)$  suppression. Thus, SHMF suppression may also be more severe in Vogelsberger et al. (2016) compared to our results because their subhalos are uniformly cored, and thus more susceptible to tides than our subhalo populations, which contain core-collapsed systems.

We compare our  $T_{\text{kd}}$ -only halo and SHMFs to our WDM simulations in Appendix B, finding that the WDM models yield  $\approx 10\%$  stronger suppression of (sub)halo abundances at our resolution limit compared to half-mode matched  $T_{\text{kd}}$  models. This is most likely due to the different slopes of the  $P(k)$  suppression in WDM versus our WSIDM models. The DAOs in our WSIDM ICs could also contribute to the difference by slightly reducing halo and subhalo abundance suppression relative to half mode-matched WDM models, although we expect this effect to be small based on the results in Paper I.

##### 4.3. $R_{\max}$ - $V_{\max}$ Relations

The  $R_{\max}$ - $V_{\max}$  relation encodes the structural properties of halos without assuming a specific density profile, and has thus been shown to effectively encode all stages of SIDM gravothermal evolution (Yang et al. 2023, 2024b; Ando et al. 2024). Figure 4 shows the isolated halo and subhalo  $R_{\max}$ - $V_{\max}$  relation in our CDM, SIDM, and  $T_{\text{kd}} = 1.46$  keV WSIDM simulations. The comparison between CDM and SIDM in the top panels is consistent with the findings in Yang et al. (2023): MilkyWaySIDM self-interactions shift a sizable fraction of low-mass isolated halos and subhalos toward larger  $V_{\max}$  and smaller  $R_{\max}$  ( $\lesssim 1$  kpc) compared to their CDM counterparts, indicating core collapse.<sup>2</sup> The remaining core-forming systems shift toward larger  $R_{\max}$  than in CDM. Note that low- $R_{\max}$  systems form a larger fraction of the to-

<sup>2</sup> The smallest values of  $R_{\max}$  we measure are comparable to the convergence radius of our simulations,  $2.8\epsilon \approx 320$  pc (Ludlow et al. 2019).

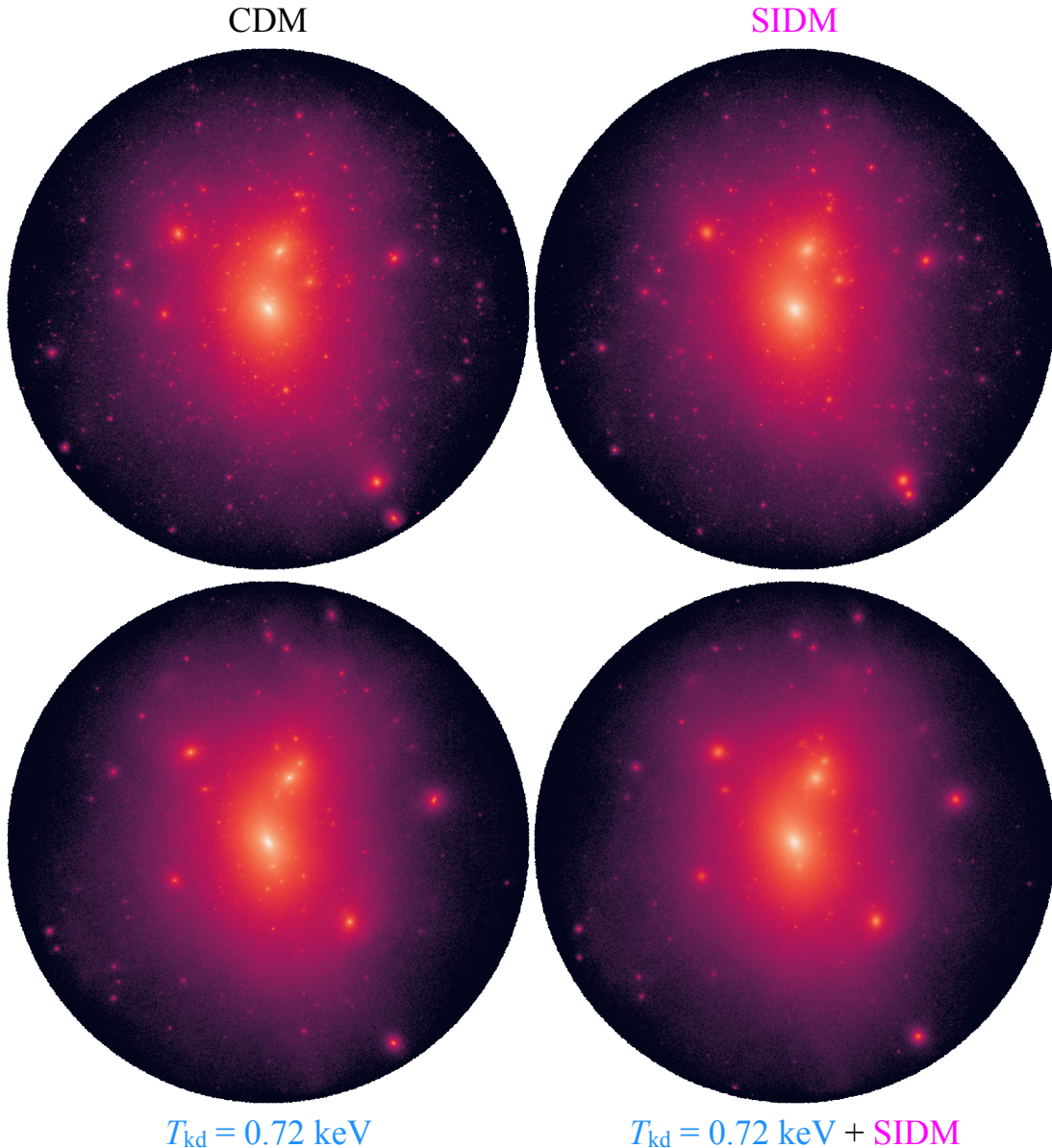


**Figure 2.** Projected DM density maps for a subset of our simulations: CDM (top left), SIDM only (top right),  $T_{\text{kd}} = 0.72$  keV  $P(k)$  suppression only (bottom left), and  $T_{\text{kd}} = 0.72$  keV WSIDM (bottom right). Each visualization is centered on the host halo and spans 1.5 times its virial radius. Visualizations were created using MESHOID (<https://github.com/mikegrudic/meshoid>).

tal subhalo (versus isolated halo) population because tidal stripping accelerates core collapse for the MilkyWaySIDM cross section (Nishikawa et al. 2020; Kahlhoefer et al. 2019; Sameie et al. 2020; Yang & Yu 2021; Zeng et al. 2022).

Introducing  $P(k)$  suppression significantly affects the  $R_{\text{max}}-V_{\text{max}}$  relation. For example, the bottom panels of Figure 4 show that (sub)halos in our  $T_{\text{kd}} = 1.46$  keV WSIDM simulation are shifted toward larger  $R_{\text{max}}$  than in SIDM. A few isolated halos and a moderate number of subhalos with small values of  $R_{\text{max}}$  remain in this WSIDM scenario, but they form a much smaller fraction of the total populations

than in SIDM. Figure 5 shows that there is a similar shift toward larger  $R_{\text{max}}$  for our  $T_{\text{kd}} = 0.72$  keV and  $T_{\text{kd}} = 2.32$  keV WSIDM simulations. In the  $T_{\text{kd}} = 0.72$  keV WSIDM simulation, low- $R_{\text{max}}$  halos are almost entirely erased. Thus, the shift toward larger  $R_{\text{max}}$  is more pronounced for models with more severe  $P(k)$  suppression (i.e., lower  $T_{\text{kd}}$ ). In addition, the suppression of the core-collapsed population is more significant for isolated halos versus subhalos when  $P(k)$  suppression is introduced.

Note that  $P(k)$  suppression *alone* contributes to the shift toward larger values of  $R_{\text{max}}$  due to the delayed formation

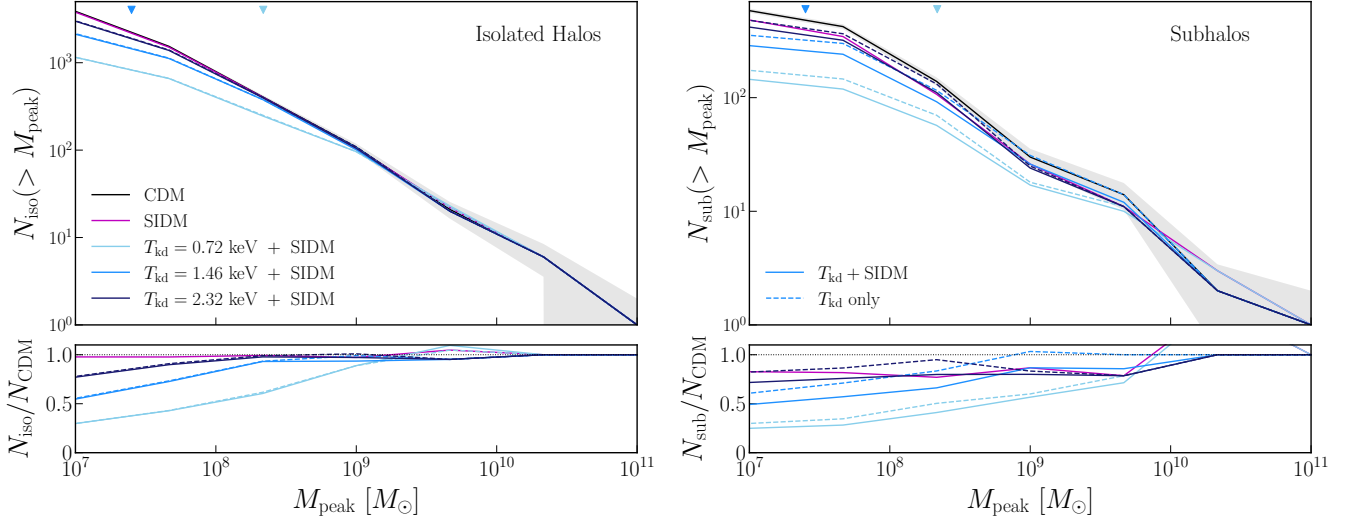


**Figure 3.** Cumulative isolated (left) and subhalo (right) mass functions, measured using (sub)halo peak virial mass and subject to a cut on present-day virial mass of  $M_{\text{vir}} > 1.5 \times 10^7 M_{\odot}$ . We compare our CDM simulation result (black) to SIDM (magenta), WSIDM (light to dark solid blue), and corresponding  $T_{\text{kd}}$ -only simulations (light to dark dashed blue). Bottom panels show ratios of cumulative subhalo abundances relative to CDM. Markers indicate the half-mode masses of the  $T_{\text{kd}} = 0.72$  and  $1.46$  keV models; the half-mode mass for  $T_{\text{kd}} = 2.32$  keV is below  $10^7 M_{\odot}$ . Gray bands show the  $1\sigma$  Poisson uncertainty on the mean cumulative CDM mass functions.

times and reduced concentrations of low-mass (sub)halos in the presence of a cutoff. This effect persists and can even be exacerbated when SIDM is included, since (sub)halos with delayed formation times are more likely to be found in the core-forming stage. This increased abundance of isolated, high- $R_{\text{max}}$  halos may help to explain the extremely low halo concentrations of gas-rich isolated ultra-diffuse galaxies (Mancera Piña et al. 2019, 2020, 2022; Kong et al. 2022). We leave this direction for future work.

#### 4.4. Gravothermal Evolution Timescales

We now use the parametric model to predict gravothermal evolution timescales following the procedure described in Section 3.3. For both isolated halos and subhalos, we apply a  $M_{\text{vir}} > 10^8 M_{\odot}$  cut to ensure that their profiles are well resolved. Figure 6 shows the normalized cumulative  $\tau_0$  distribution for isolated halos (left) and subhalos (right). As  $P(k)$  suppression is introduced and becomes more severe, the fraction of core-forming isolated halos increases approximately linearly across our models. The subhalo  $\tau_0$  distribution is affected in a less regular fashion, particularly when comparing our SIDM, and  $T_{\text{kd}} = 1.46$  and  $2.32$  keV WSIDM results. This is consistent with the difference in  $R_{\text{max}}-V_{\text{max}}$  relations we observed for subhalos versus isolated halos in Section 4.3, and further confirms that linear  $P(k)$  suppression and nonlinear subhalo evolution physics affect (sub)halos’ gravothermal evolution in a nontrivial manner; we study these coupled effects further in Section 5.

The fraction of core-collapsed subhalos (isolated halos) with  $M_{\text{vir}} > 10^8 M_{\odot}$  in our SIDM simulation is 18% (13%), consistent with the results in Yang et al. (2023). The core-collapsed fraction is expected to peak at roughly  $10^8 M_{\odot}$ , which corresponds to the velocity scale  $w$  of the turnover in

the underlying SIDM cross section (Ando et al. 2024). In our  $T_{\text{kd}} = 0.72$ ,  $1.46$ , and  $2.32$  keV models, we predict that these subhalo (isolated halo) core-collapsed fractions become 2% (2%), 8% (2%), and 17% (4%), respectively.

For isolated halos, these changes to the core-collapsed fraction primarily probe suppression in halo growth histories (and thus concentrations) due to  $P(k)$ . Since  $\tau_0$  depends strongly on halo concentration, even the  $T_{\text{kd}} = 2.32$  keV suppression is sufficient to delay core-collapse in nearly all isolated halos we resolve. Meanwhile, the core-collapsed fraction for subhalos is sensitive to the correlated effects of growth history and tidal stripping. Since core-collapsed subhalos are more resistant to tidal disruption than cored systems, the subhalo core-collapsed fraction is less sensitive to  $P(k)$  suppression for the coldest models we simulate.

### 5. THE INTERPLAY BETWEEN $P(k)$ SUPPRESSION AND GRAVOTHERMAL EVOLUTION

We now study the physical drivers of WSIDM (sub)halos’ gravothermal evolution. When comparing our WSIDM and SIDM simulations, two main effects are at play:

1. Some low-mass (sub)halos that core collapse in SIDM (without  $P(k)$  suppression) do not form in WSIDM;
2. Some (sub)halos that core collapse in SIDM have delayed and/or suppressed growth histories in WSIDM, preventing core collapse.

To assess the impact of the first effect (i.e., the erasure of low-mass (sub)halos), we fit “effective” WDM models that match the total halo and subhalo abundances in our  $T_{\text{kd}}$ -only simulations, using the WDM SHMF suppression fit derived in Paper I (see Appendix B for details). For simplicity, we assume this fit also applies to the isolated halo



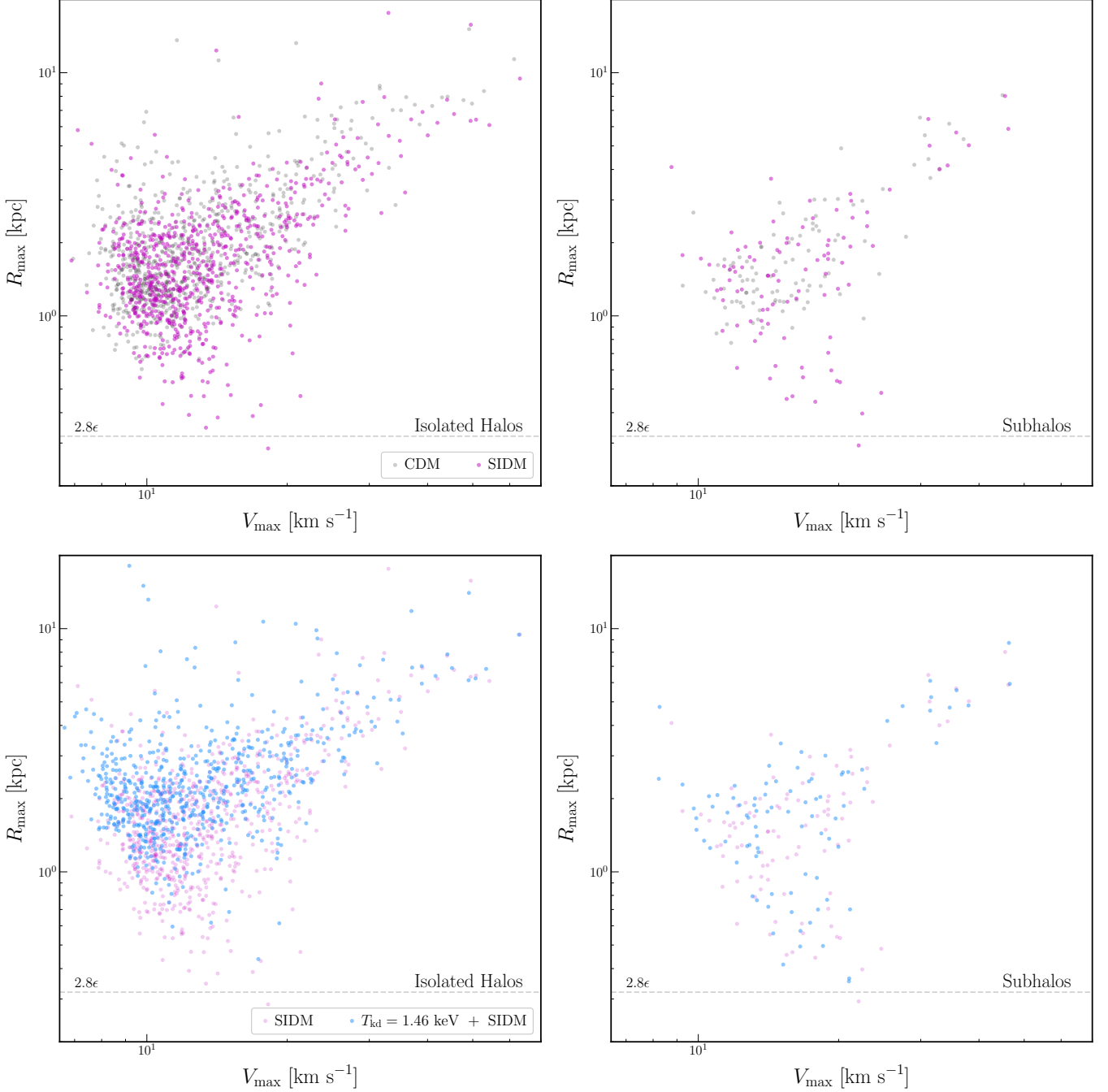


**Figure 4.** The relation between maximum circular velocity,  $V_{\max}$ , and the radius at which  $V_{\max}$  is achieved,  $R_{\max}$ , for isolated halos (left column) and subhalos (right column). Results are shown for our CDM simulation (gray), our SIDM simulation with CDM ICs (magenta), and our SIDM simulation with  $T_{\text{kd}} = 1.46$  keV ICs (blue).

mass function suppression. We derive effective thermal-relic WDM masses of  $m_{\text{WDM}} = 4.2$  (5.3), 6.9 (7.9), and 10.2 (11.3) keV for subhalos (isolated halos) in our  $T_{\text{kd}} = 0.72$  and 1.46, and 2.32 keV simulations, respectively. These values are slightly larger than the masses of the corresponding half-mode-matched WDM models due to differences in the shape of the transfer function cutoff and/or the low-amplitude DAOs in our  $T_{\text{kd}}$  models, as discussed in Section 4.2.

We apply this suppression to re-weight predicted  $\tau_0$  distribution from our SIDM simulation, based on (sub)halos'  $M_{\text{peak}}$  values. These results, shown by the faint dashed lines in Figure 6, are nearly identical to the SIDM (magenta) result for isolated halos. Thus, the erasure of low-mass systems has a minor effect on the  $\tau_0$  distributions, consistent with our conclusion above that the isolated halo core-collapsed fraction is primarily sensitive to halo growth histories. For subhalos,

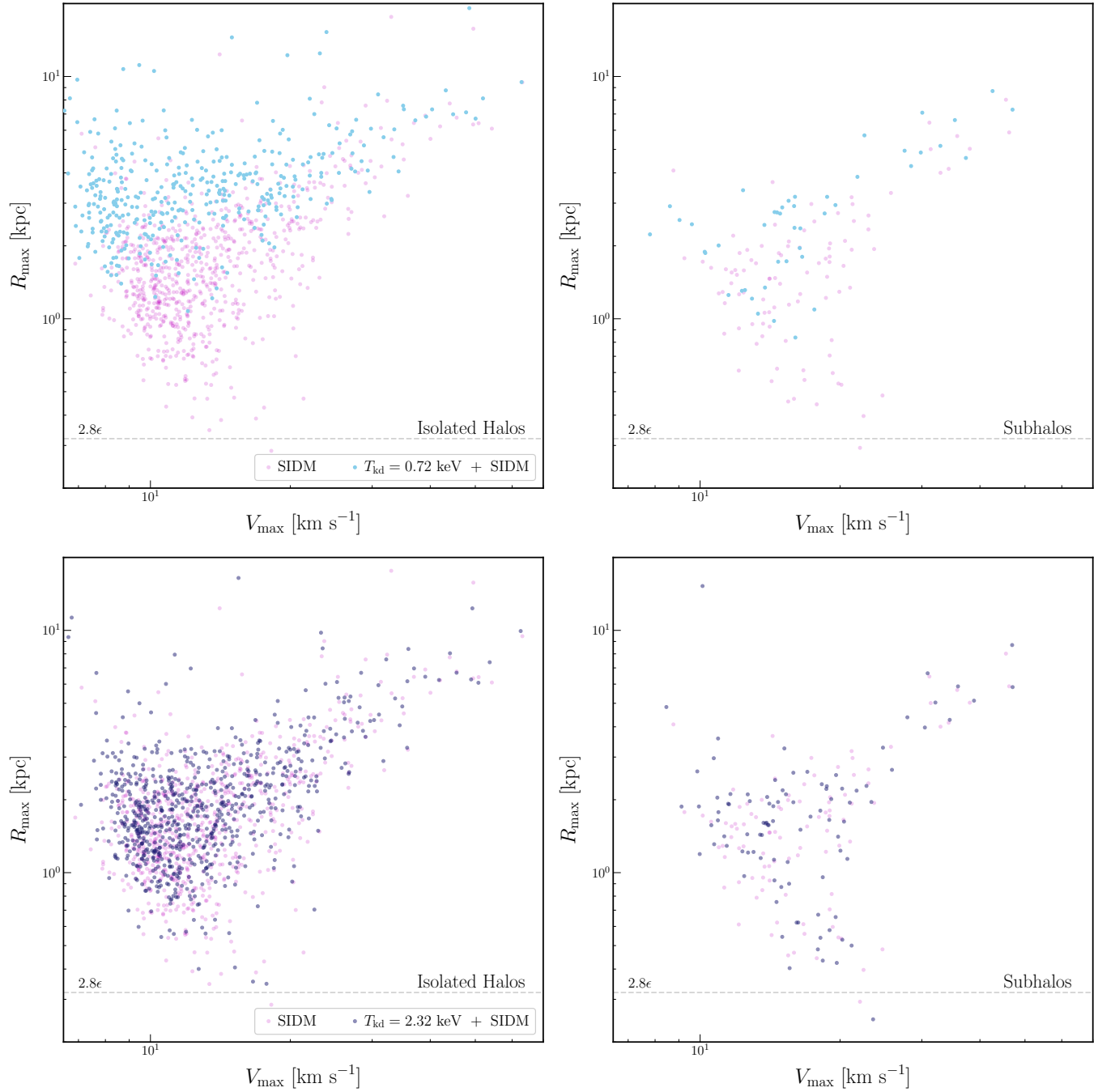


**Figure 5.** Same as Figure 4, for our WSIDM simulation with  $T_{\text{kd}} = 0.72$  keV (top) and 2.32 keV (bottom); in addition, both panels show the result for our SIDM simulation (magenta).

the erasure of low-mass systems explains about half of the shift in the  $T_{\text{kd}} = 0.72$  keV WSIDM  $\tau_0$  distribution relative to SIDM; the shift is smaller for  $T_{\text{kd}} = 1.46$  and 2.32 keV.

To assess the impact of the second effect (delayed and suppressed growth), we match subhalos between our simulations based on their orbital and  $V_{\text{max}}$  histories. Figure 7 illustrates the evolution of three representative pairs of matched subhalos from our CDM, SIDM, and  $T_{\text{kd}} = 1.46$  keV simulations with and without self-interactions:

- The high-mass subhalo (top row) has a slightly delayed merger history and suppressed  $V_{\text{max}}$  evolution in our  $T_{\text{kd}}$ -only simulation, relative to CDM. In SIDM, its final value of  $V_{\text{max}}$  is slightly enhanced relative to CDM and similar to the WSIDM result.
- The moderate-mass subhalo (middle row) is core-collapsed in our SIDM simulation, signaled by its steeply-rising  $V_{\text{max}}$  evolution at late times relative to

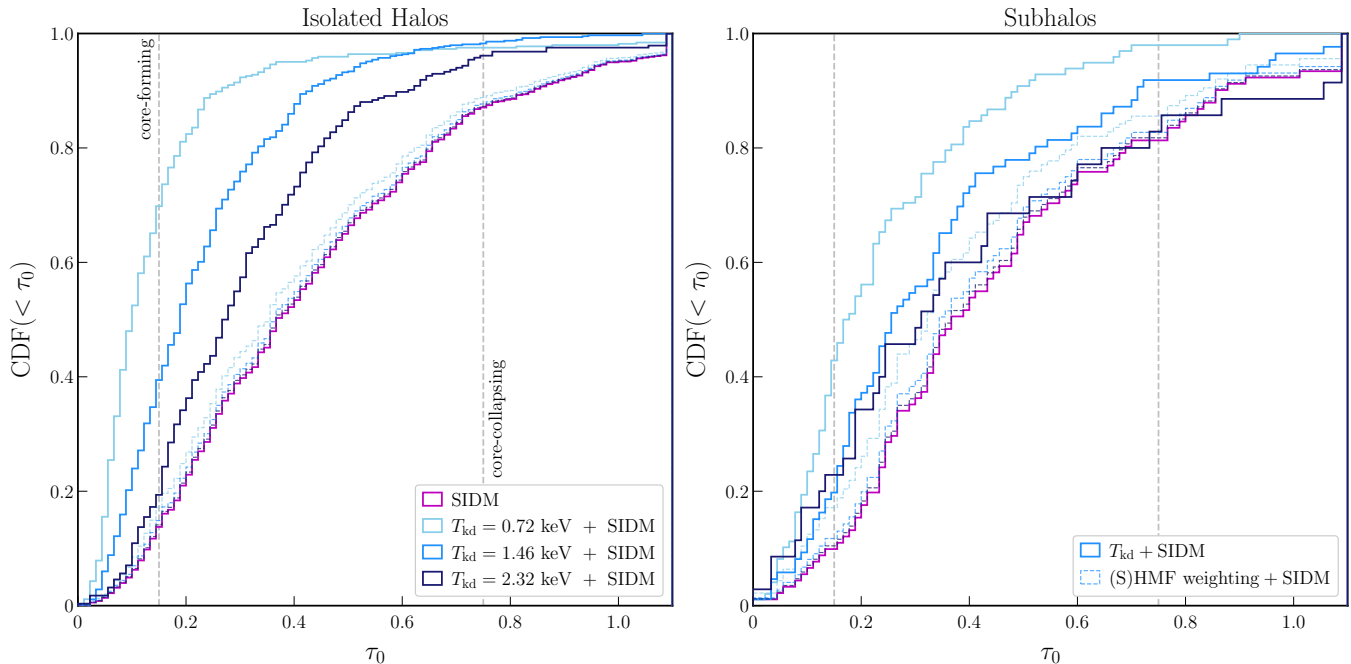


**Figure 6.** Normalized cumulative distributions of the gravothermal evolution timescale,  $\tau_0$ , for isolated halos (left) and subhalos (right) with  $M_{\text{vir}} > 10^8 M_{\odot}$  in our SIDM (magenta) and  $T_{\text{kd}} = 0.72, 1.46,$  and  $2.32$  keV WSIDM simulations (thick solid lines). The gravothermal evolution timescale  $\tau_0$  is calculated using the parametric SIDM model from Yang et al. (2024b,a), and clipped at a maximum value of 1.1; see Section 3.3 for details. Systems with  $\tau_0 < 0.15$  (left dashed vertical line) are in the core expansion phase; systems with  $\tau_0 > 0.75$  (right dashed vertical line) are deep in the core-collapsed phase, with a rapidly-increasing central density that exceeds its original value. In both panels, thick solid lines show the WSIDM simulation result, while thin dashed lines show the SIDM  $\tau_0$  distribution weighted by the probability that (sub)halos form in each  $T_{\text{kd}}$  model based on an effective mapping to WDM (see Section 5).

CDM. This subhalo is less collapsed in our WSIDM simulation, while its  $V_{\text{max}}$  history is suppressed in our  $T_{\text{kd}}$ -only simulation. Mass loss rates in our SIDM and WSIDM simulations are slightly enhanced relative to CDM. In addition, its orbital phase shifts in the  $T_{\text{kd}}$  simulations with and without self-interactions.

- The low-mass subhalo (bottom row) has a significantly suppressed (and mildly delayed)  $V_{\text{max}}$  evolution history in the  $T_{\text{kd}} = 1.46$  keV-only WSIDM run relative to CDM. In SIDM, this subhalo is core-collapsed (evidenced by its enhanced  $V_{\text{max}}$  relative to CDM). In WSIDM, its  $V_{\text{max}}$  is suppressed at early times but nearly catches up to CDM at late times, while the  $T_{\text{kd}}$ -only version retains a lower  $V_{\text{max}}$  throughout its history.

Thus, introducing  $P(k)$  suppression can delay or even erase core collapse. In our  $T_{\text{kd}} = 1.46$  keV WSIDM simulation, this is mainly due to the reduced concentration of WSIDM (sub)halos, which systematically achieve lower values of  $V_{\text{peak}}$  than in CDM. Crucially, (sub)halos' early evolution histories significantly affect their subsequent gravothermal evolution, as the core-collapse timescale is extremely sensitive to halo concentration (Essig et al. 2019; Nadler et al. 2023a). As a result, two competing effects—core collapse driven by SIDM and suppressed growth driven by  $P(k)$ —can roughly

cancel for some (sub)halos, resulting in present-day  $V_{\text{max}}$  values similar to CDM.

We also show matched subhalo evolution histories for  $T_{\text{kd}} = 0.72$  and  $2.32$  keV in Appendix C. In the  $T_{\text{kd}} = 0.72$  keV case, WSIDM subhalo evolution histories are substantially suppressed *and* delayed relative to SIDM. Thus, in addition to the effects of reduced concentration discussed above, gravothermal evolution in models with extreme  $P(k)$  suppression has less time to operate, further reducing the core-collapsed fraction. Meanwhile, in the  $T_{\text{kd}} = 2.32$  keV case, the delay is negligible and the reduced halo concentration effect dominates over delayed growth. Beyond the examples shown in Figure 7 and Appendix C, we have verified that these conclusions are robust by inspecting the  $V_{\text{max}}$  histories of all matched subhalos above our resolution limit. In future work, it will be important to study how the effects discussed above propagate to (sub)halos' full density profiles.

Finally, we note that the tidal evolution of WSIDM subhalos can differ from that of matched SIDM subhalos; in turn, this can alter their gravothermal evolution. In particular, tidal evolution can be affected by changes to the host potential and/or subhalo density profiles between SIDM and WSIDM models. In Appendix E, we show that the MW host's density profile is nearly identical in our SIDM and WSIDM simulations, indicating that the latter effect is more important given our SIDM cross section.

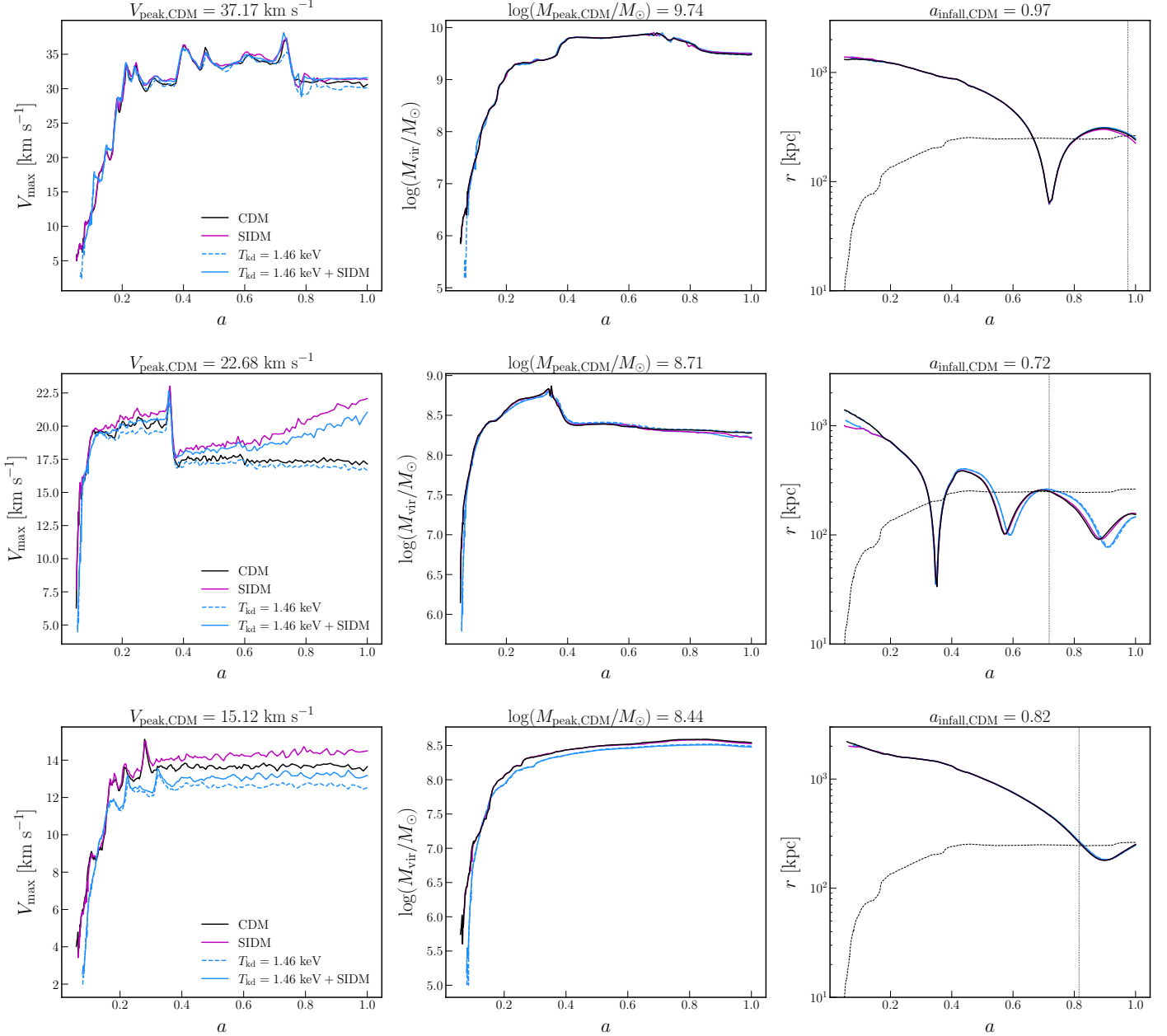


**Figure 7.** Evolution of maximum circular velocity  $V_{\max}$  (left), virial mass  $M_{\text{vir}}$  (middle), and distance from the host center  $r$  (right) versus scale factor  $a$  for matched subhalos. Results for a high (top), medium (middle), and low-mass (bottom) subhalo are shown for CDM (black), SIDM (magenta),  $T_{\text{kd}} = 1.46$  keV WSIDM (blue), and  $T_{\text{kd}} = 1.46$  keV-only (dashed blue). In the right column, the dashed black line shows the MW host’s virial radius, and the vertical dotted line shows the scale factor of each subhalo’s most recent infall into the host,  $a_{\text{infall}}$ .

## 6. PREDICTIONS FOR DWARF GALAXY SUBHALOS

We now study the density profiles (Section 6.1) and central density–pericenter relation (Section 6.2) of subhalos that are expected to host dwarf galaxies in our simulations. Throughout this Section, we study the  $T_{\text{kd}} = 1.46$  keV model because it is closest to the current WDM constraint from MW satellite galaxy population derived by Nadler et al. (2021b); we show results for other  $T_{\text{kd}}$  models in Appendix D. We focus on subhalos, with an eye toward modeling MW satellite galaxies.

We use the abundance-matching model from Nadler et al. (2019b, 2020b, 2024b), with best-fit parameters inferred from Dark Energy Survey and Pan-STARRS1 MW satellite observations (Drlica-Wagner et al. 2020; Nadler et al. 2020b), to predict the luminosity of the satellite galaxy hosted by each subhalo as a function of its peak maximum circular velocity,  $V_{\text{peak}}$ . We measure  $V_{\text{peak}}$  using only snapshots prior to infall, rather than all snapshots, to avoid increases in predicted luminosity due to late-time increases in  $V_{\text{max}}$  for core-collapsed SIDM and WSIDM subhalos.

Following Nadler et al. (2024b), we do not alter the galaxy–halo connection model in our beyond-CDM simulations. We leave a study of the coupling between  $P(k)$  suppression, SIDM effects, and the galaxy–halo connection to future work.

### 6.1. Subhalo Density Profiles

Figure 8 shows subhalo density profiles (left) and circular velocity profiles (right) in our CDM (top), SIDM (middle), and  $T_{\text{kd}} = 1.46$  keV WSIDM (bottom) simulations. We restrict to the 30 highest- $V_{\text{peak}}$  subhalos because  $V_{\text{peak}}$  correlates with luminosity in our abundance-matching model; this cut therefore roughly selects the most easily detectable systems. We also impose  $M_{\text{sub}} > 1.2 \times 10^8 M_{\odot}$  at  $z = 0$  before selecting these 30 subhalos in each run. The colormap indicates the abundance matching-predicted luminosity, and the magenta line corresponds to the LMC analog in each simulation.

In CDM, we find a uniformly cuspy distribution of subhalo density profile slopes, and a spread of  $\mathcal{O}(1)$  dex about the mean inner density profile amplitude. Density profile amplitudes at small radii ( $r \lesssim 1$  kpc) correlate with peak subhalo maximum circular velocity, and thus with luminosity (which is set by  $V_{\text{peak}}$  in our abundance-matching model). On the other hand, in our SIDM simulation, high-mass subhalos have  $\mathcal{O}(\text{kpc})$  density cores, while subhalos with  $M_{\text{sub}} \lesssim 10^9 M_{\odot}$  (i.e.,  $L \lesssim 10^5 L_{\odot}$ ; Nadler et al. 2020b) have a range of density profile shapes, ranging from large cores to very cuspy inner profiles for core-collapsed objects. Thus, self-interactions diversify subhalo density profile amplitudes and slopes, thereby changing the relation between predicted densities and expected dwarf galaxy luminosities.

The bottom row of Figure 8 shows that introducing  $P(k)$  suppression at the level currently probed by MW satellite abundances removes some of the lowest-mass subhalos that core collapse in our SIDM simulation, and erases the core-collapse signature in others. In addition, a few higher-mass subhalos that did not collapse in our SIDM simulation have very steep density profiles in our WSIDM run, indicating that detailed changes to the merger and/or orbital histories caused by altering the ICs can accelerate core collapse for specific subhalos, even though it is inhibited in general for WSIDM systems (see Section 5). Overall, the effect of  $P(k)$  suppression on subhalo profiles is mild for the  $T_{\text{kd}} = 1.46$  keV model. We show the  $T_{\text{kd}} = 0.72$  keV WSIDM result in Appendix D.1, which is more extreme and results in only a few core-collapsed (sub)halos. Meanwhile, the distribution of subhalo profiles in our  $T_{\text{kd}} = 2.32$  keV WSIDM simulation is very similar to that in SIDM.

These CDM, SIDM, and WSIDM results are reflected in the corresponding circular velocity profiles and are consistent with the CDM and SIDM results from Yang et al. (2023). For reference, we show circular velocity measurements for observed classical and ultra-faint MW satellites as compiled by Silverman et al. (2023) in the circular velocity panels. The data are generally consistent with the high-amplitude cuspy profiles in our CDM simulation and the core-collapsed subhalos in our SIDM and WSIDM simulations. However, these

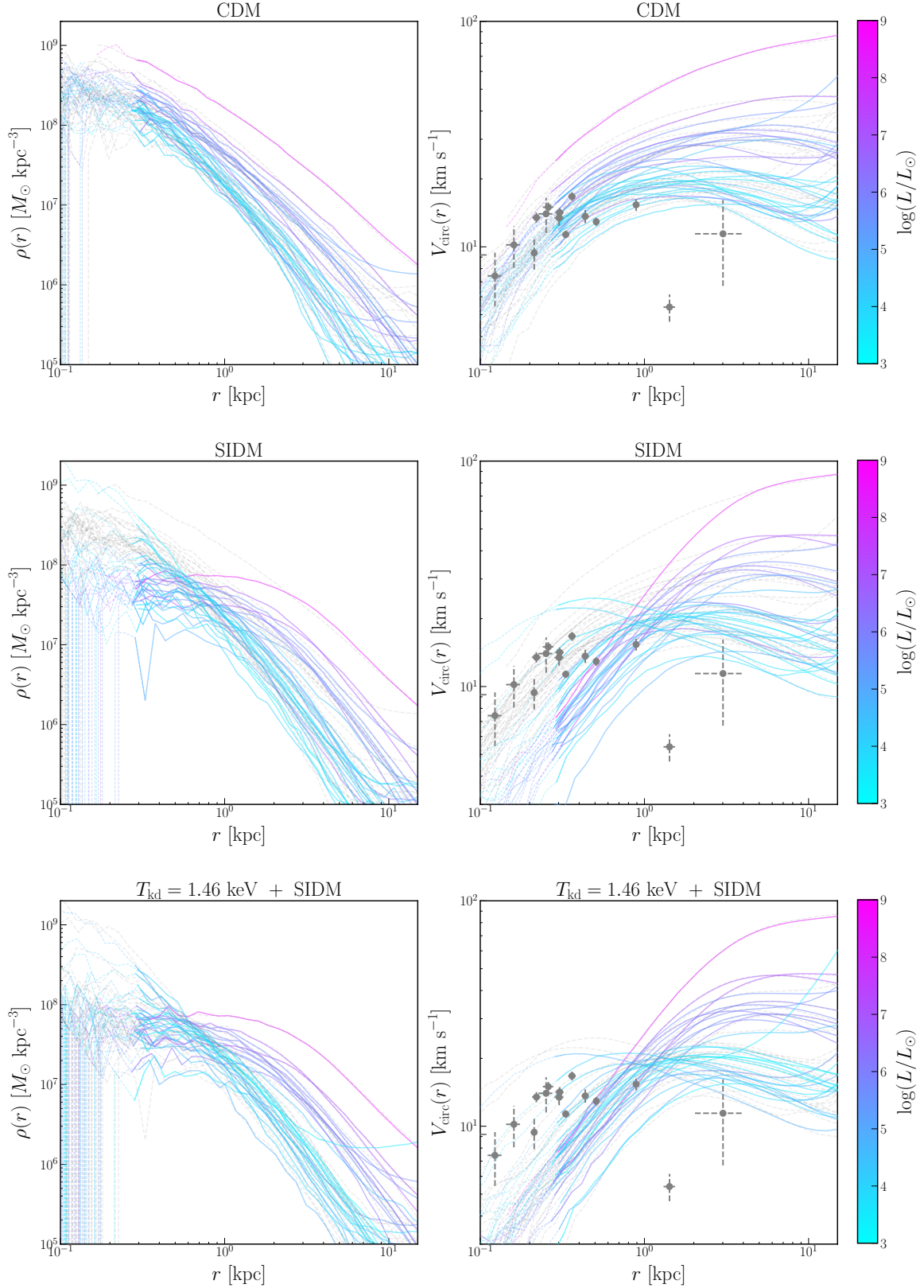
comparisons are qualitative, and detailed forward modeling of satellites’ observed stellar velocity dispersions and sizes, in the presence of a realistic MW disk potential, are needed to quantitatively constrain SIDM and WSIDM models.

### 6.2. Central Density–Pericenter Relation

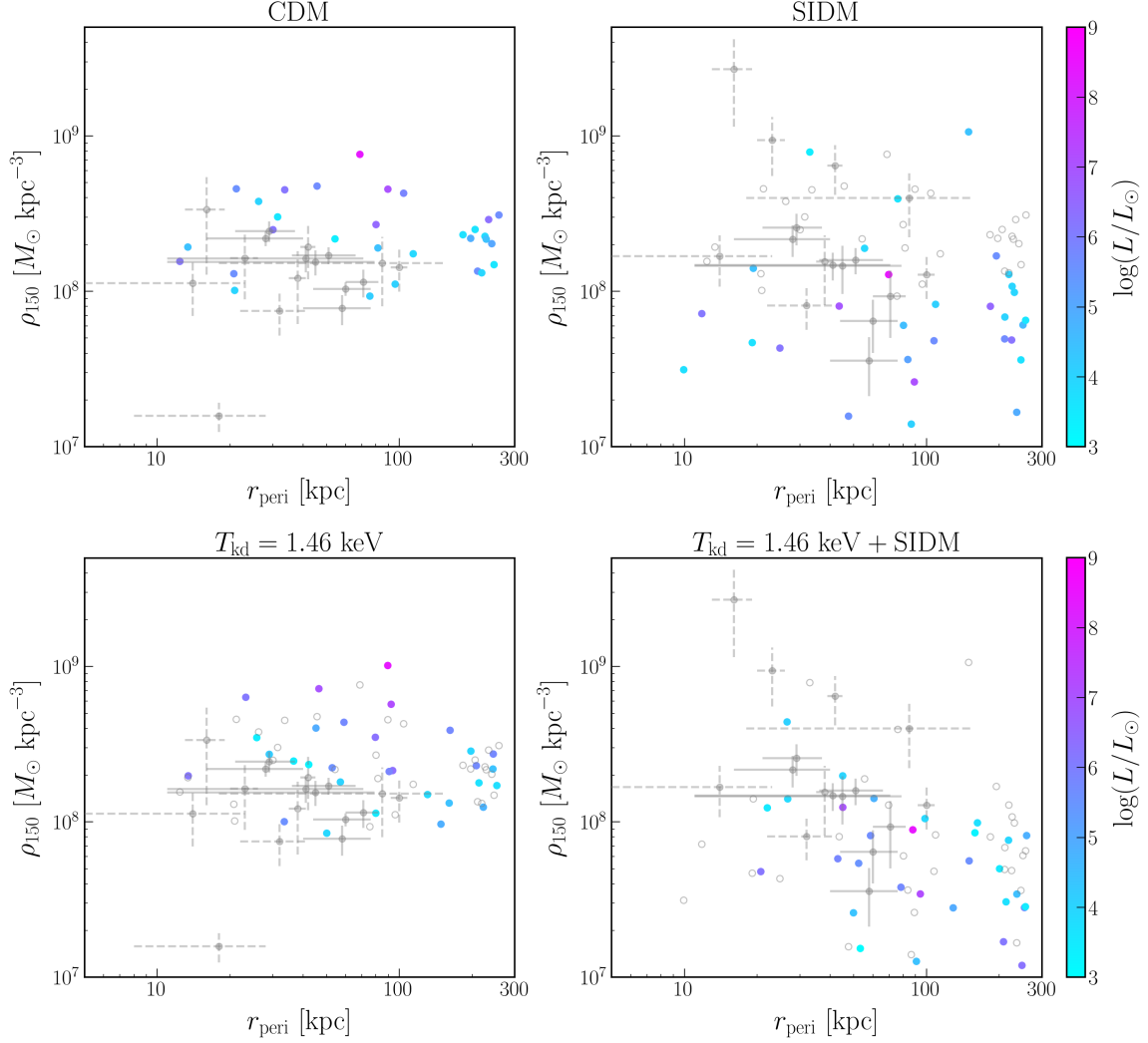
Tidal stripping can accelerate gravothermal evolution (e.g., Nishikawa et al. 2020; Sameie et al. 2020; Zeng et al. 2022). Thus, it is important to consider the orbital properties of observed satellites when interpreting their central densities in the context of SIDM and WSIDM. For example, Kaplinghat et al. (2019) and Andrade et al. (2024) reported an anticorrelation between observed satellites’ orbital pericenters and central densities (however, see Cardona-Barrero et al. 2023). To evaluate this relation for subhalos in our simulations, we measure  $\rho_{150}$ —the central density at a radius of 150 pc from each subhalo’s center—because many of the observed satellites’ central densities have been measured at this radius (e.g., Pace et al. 2022). Although 150 pc is slightly below our simulations’ formal convergence radius, our density profile measurements in Figure 8 indicate that central densities do not vary drastically for most subhalos between 150 pc and  $2.8\epsilon = 320$  pc. We measure each subhalo’s pericenter,  $r_{\text{peri}}$ , as the smallest distance it achieves relative to the host across all snapshots using a cubic spline fit to subhalo and host three-dimensional positions. We again restrict to the 30 highest- $V_{\text{peak}}$  subhalos with  $M_{\text{vir}} > 1.2 \times 10^8 M_{\odot}$  in each simulation.

Figure 9 shows the  $\rho_{150}$ – $r_{\text{peri}}$  relation in our CDM, SIDM, and  $T_{\text{kd}} = 1.46$  keV simulations with and without self-interactions; we again restrict to the 30 highest- $V_{\text{peak}}$  subhalos in each simulation. These quantities are not significantly correlated in most of our runs. To quantify this, we calculate Spearman rank correlation coefficients  $\rho$  and  $p$ -values; the coefficient  $\rho$  measures the correlation strength between ranked variables, with +1 (–1) representing perfect correlation (anticorrelation). These tests yield  $p > 0.05$  in all cases except our  $T_{\text{kd}} = 0.72$  and 1.46 keV WSIDM runs. In these two WSIDM simulations, combining  $P(k)$  suppression and self-interactions boosts the anticorrelation strength relative to SIDM or  $T_{\text{kd}}$ -only runs, yielding a Spearman statistic of  $\rho = -0.47$  and  $p = 0.01$  in both cases. This boost is due to the presence of both core-forming and collapsing subhalos at low  $r_{\text{peri}}$ , as well as a population of extremely low- $\rho_{150}$  subhalos with large  $r_{\text{peri}}$  (see Section 7.3 for further discussion). Similar results hold when comparing our CDM and SIDM simulations (consistent with the findings of Yang et al. 2023) and our other  $T_{\text{kd}}$ -only and WSIDM models, but our SIDM and  $T_{\text{kd}} = 2.32$  keV WSIDM simulations do not produce statistically significant anticorrelations. See Appendix D.2 for  $T_{\text{kd}} = 0.72$  and 2.32 keV results.

Figure 9 also shows observed classical and ultra-faint satellites’ derived  $\rho_{150}$  and  $r_{\text{peri}}$  values, as compiled in Kaplinghat et al. (2019). Observed satellites with both high and low central densities exist, particularly at small  $r_{\text{peri}}$ ; this is even more noticeable when their density profiles are inferred using an isothermal profile. SIDM and WSIDM qualitatively reproduce the observed central density diversity due



**Figure 8.** Density profiles (left) and circular velocity profiles (right) of the 30 highest- $V_{\text{peak}}$  subhalos with  $M_{\text{vir}} > 1.2 \times 10^8 M_\odot$  in our CDM (top), SIDM (middle), and  $T_{\text{kd}} = 1.46 \text{ keV}$  WSIDM (bottom) simulations. Faint gray lines in the top, middle, and bottom rows respectively show  $T_{\text{kd}} = 1.46 \text{ keV}$ -only, CDM, and SIDM results. Subhalos are colored by the luminosities of the dwarf galaxies they are predicted to host using the Nadler et al. (2020b) abundance-matching model. Lines transition to dashed below our convergence radius of  $2.8\epsilon = 320 \text{ pc}$ .  $V_{\text{circ}}$  measurements at the half-light radius for observed MW satellites, as compiled in Silverman et al. (2023), are shown for the nine classical satellites ( $L > 10^5 L_\odot$ ; solid error bars), and a subset of known ultra-faint dwarfs ( $L < 10^5 L_\odot$ ; dashed error bars).



**Figure 9.** Distribution of central density evaluated at 150 pc,  $\rho_{150}$ , versus pericentric distance,  $r_{\text{peri}}$ , for the 30 highest- $V_{\text{peak}}$  subhalos with  $M_{\text{sub}} > 1.2 \times 10^8 M_{\odot}$  in our CDM (top left), SIDM (top right),  $T_{\text{kd}} = 1.46$  keV-only (bottom left), and  $T_{\text{kd}} = 1.46$  keV WSIDM (bottom right) simulations. Open gray circles in the top right and bottom left panels (bottom right panel) show the CDM (SIDM) result. Subhalos are colored by the luminosities of the dwarf galaxies they are predicted to host using the Nadler et al. (2020b) abundance-matching model. Derived  $\rho_{150}$  and  $r_{\text{peri}}$  values for observed MW satellites, as compiled in Kaplinghat et al. (2019), are shown for the nine classical satellites ( $L > 10^5 L_{\odot}$ ; solid error bars) and a subset of known ultra-faint dwarfs ( $L < 10^5 L_{\odot}$ ; dashed error bars). These central densities are derived assuming Navarro–Frenk–White (NFW; Navarro et al. 1997) profiles appropriate for CDM and  $T_{\text{kd}}$ -only models in the left panels, and isothermal profiles appropriate for SIDM and WSIDM models in the right panels.

to the existence of both cored and core-collapsed subhalos. In contrast, Ebisu et al. (2022) show that velocity-independent SIDM with  $\sigma_0/m_{\chi} \sim 1$  to  $3 \text{ cm}^2 \text{ g}^{-1}$  uniformly reduces subhalos’ central densities, rather than mimicking the observed spread in the  $\rho_{150}$ – $r_{\text{peri}}$  relation, because core collapse does not occur in these scenarios. Similar to Figure 8, quantitative comparisons to our simulation predictions will require forward modeling satellites’ velocity dispersions and orbits, including measurement systematics. In parallel, it will be important to scrutinize our results using improved subhalo finders that track highly stripped subhalos (e.g., SYMFIND; Mansfield et al. 2024) and by running

SIDM and WSIDM extensions of embedded disk simulation suites (e.g., EDEN; Wang et al. 2024). In particular, the MW disk may disrupt core-forming subhalos with small pericentric distances, thereby increasing the anti-correlation central density–pericenter anti-correlation; we return to this point in Section 7.3.

## 7. DISCUSSION

We now discuss our results, focusing on the implications of  $P(k)$  suppression for core collapse in our WSIDM simulations (Section 7.1), comparison to previous work and partic-

ularly ETHOS simulations (Section 7.2), and areas for future work associated with our setup and analyses (Section 7.3).

### 7.1. Core Collapse in WSIDM

Core collapse is a distinct signature of SIDM models. If DM self-interactions significantly impact the inner density profiles of subhalos that host MW satellite galaxies, core collapse is needed in a significant fraction of these systems to avoid under-predicting their central densities (e.g., Silverman et al. 2023). As discussed in Section 6.2, this conclusion is strengthened when considering the orbital properties of observed MW satellites. In particular, SIDM models that uniformly core MW subhalos, rather than producing core collapse in a fraction of these systems, yield subhalo populations that are not sufficiently diverse to account for the observed distribution of MW satellite central densities and pericenters (e.g., Ebisu et al. 2022). This situation motivates a strong, velocity-dependent cross section (Correa 2021; Yang et al. 2023). Similar conclusions hold when dwarfs’ stellar velocity dispersions are modeled directly (e.g., Kim & Peter 2021).

For a wide range of SIDM models encapsulated by Equation 1, the velocity-dependent cross sections with large  $\sigma_0/m_\chi$  needed to achieve core collapse are naturally accompanied by a cutoff in  $P(k)$ . This cutoff affects the formation and evolution of low-mass (sub)halos, which are precisely the systems expected to core collapse in the absence of  $P(k)$  suppression. By simulating three benchmark models with varying levels of  $P(k)$  suppression, we find that WSIDM (sub)halo population statistics vary depending on the amplitude of  $P(k)$  suppression; furthermore, WSIDM can differentially impact isolated halos versus subhalos relative to SIDM. Focusing on the core-collapsed population, we highlight the following conclusions from our results:

- In the model featuring the most extreme suppression in the linear power spectrum ( $T_{\text{kd}} = 0.72$  keV), roughly half of the (sub)halos that collapse in our SIDM simulation never form (Figures 3 and 5); the remaining systems’ growth histories are heavily delayed and suppressed. These effects combine to nearly entirely remove the core-collapse signature.
- As the power spectrum cutoff moves to smaller scales ( $T_{\text{kd}} = 1.46$  keV), (S)HMF suppression weakens (Figure 3). However, the core-collapsed fraction is still significantly reduced because low-mass (sub)halos’ growth is suppressed (and mildly delayed) relative to simulations without a  $P(k)$  cutoff (Figures 6 and 7).
- For a  $P(k)$  cutoff at even smaller scales ( $T_{\text{kd}} = 2.32$  keV), the (S)HMF is weakly suppressed (Figure 3) but the core-collapsed population is still moderately suppressed relative to SIDM (Figure 6). This illustrates the extreme sensitivity of gravothermal evolution to (sub)halo growth histories.

In all cases, this reduction of the population of core-collapsed systems is more severe for isolated halos com-

pared to subhalos (e.g., see Figure 6), likely because subhalos’ gravothermal evolution is accelerated by tidal stripping whereas isolated halos’ gravothermal evolution is (to first order) determined by their accretion of lower-mass objects, which probe  $P(k)$  on smaller scales.

### 7.2. Comparison to Previous Work

Several authors have considered the direct impact of DM self-interactions on  $P(k)$ . For example, early studies by Atrio-Barandela & Davidson (1997); Hannestad & Scherrer (2000) found that certain SIDM models (e.g., involving a massive vector boson mediator) slightly reduce small-scale  $P(k)$  suppression relative to a corresponding WDM model (also see Atrio-Barandela & Davidson 2001). Recent work that considers a wider range of SIDM models reach similar conclusions in linear theory (e.g., Huo 2020; Yunis et al. 2020, 2022; Egana-Ugrinovic et al. 2021; Garani et al. 2022). In our WSIDM models, power spectrum suppression is slightly steeper than in the corresponding thermal-relic WDM models with equal half-mode scales, and there are low-amplitude DAOs below the initial cutoff. Both features are consistent with the general picture outlined by previous work.

To our knowledge, the only previous simulations that include both  $P(k)$  suppression and DM self-interactions were also run in the ETHOS framework (Cyr-Racine et al. 2016). We focus on comparing to Vogelsberger et al. (2016), since their simulation resolution and zoom-in setup is broadly similar to ours. These authors consider ETHOS models that roughly match the half-mode scales of 1.89, 2.67, and 3.66 keV thermal-relic WDM, with SIDM cross sections that are comparable to our MilkyWaySIDM model. Thus, their least suppressed model is similar to our most suppressed  $T_{\text{kd}} = 0.72$  keV scenario, which is half-mode matched to  $m_{\text{WDM}} = 3.5$  keV. As we have shown,  $P(k)$  suppression is so strong in this model that core collapse is almost entirely eliminated, even though it would be achieved with CDM ICs. This is due to both the erasure of low-mass subhalos and their delayed and suppressed growth. Subhalo maximum circular velocity functions in Vogelsberger et al. (2016) are uniformly suppressed relative to a CDM simulation without self-interactions, consistent with this interpretation. Our study therefore complements Vogelsberger et al. (2016) by including models with sufficiently mild  $P(k)$  suppression to preserve core collapse.

### 7.3. Future Work

We have presented DM-only zoom-in simulations of a MW analog in CDM, SIDM, and WSIDM. There are several areas for future work and potential caveats: host-to-host variance, subhalo finding, convergence of (sub)halos’ gravothermal evolution, and the impact of baryons.

First, regarding host-to-host variance, we expect WSIDM (S)HMF suppression relative to CDM to be similar across MW zoom-in environments because it is determined by the small-scale  $P(k)$  cutoff. For example, Paper I showed that WDM SHMF suppression is consistent across three different



MW hosts. Predictions for absolute (sub)halo abundances depend on host mass, accretion history, and environment; modeling WSIDM effects in large samples of MW analogs will therefore be important. We note that Meshveliani et al. (2024) measured an environmental dependence of WDM halo mass function suppression across a cosmological volume that includes underdense regions, which our zoom-ins avoid by construction. It will be interesting to model this effect in the Local Volume using constrained simulations (Carlesi et al. 2016; McAlpine et al. 2022; Wempe et al. 2024).

Second, regarding subhalo finding, we have used the ROCKSTAR halo finder and CONSISTENT-TREES merger tree codes (Behroozi et al. 2013a,b), which are known to prematurely lose track of certain subhalos in CDM. This effect is most severe for highly-stripped subhalos near hosts' centers, but can persist even for (initially) massive systems (Mansfield et al. 2024). In SIDM and WSIDM, many subhalos are cored at infall, and it is possible for tides to completely unbind these systems (e.g., Errani et al. 2023). On the other hand, it is more challenging to reliably identifying cored versus cuspy subhalos, although this has not been thoroughly studied. Thus, it is possible that the  $\mathcal{O}(10\%)$  subhalo abundance suppression we measure due to self-interactions (Figure 3, right panel) is partly due to incomplete subhalo finding. Nonetheless, we demonstrate that our main results are converged in Appendix A, and we have focused on comparisons between SIDM and WSIDM that mitigate this systematic.

Third, regarding convergence of our SIDM and WSIDM (sub)halo density profiles, recent studies highlight a set of related challenges: finite particle resolution can add artificial scatter to predicted collapse times, extremely low-concentration or core-collapsed subhalos can be systematically mis-modeled, and the self-interaction algorithm and/or simulation parameters (e.g., time-stepping and softening) can bias predictions (Zhong et al. 2023; Palubski et al. 2024; Mace et al. 2024; Fischer et al. 2024). We find very few of the extremely low-concentration (sub)halos that Mace et al. (2024) show are particularly difficult to simulate; meanwhile, our core-collapsed (sub)halos' central densities are typically enhanced relative to CDM by an  $\mathcal{O}(1)$  factor, which implies that these systems are not in the deeply core-collapsed phase where simulations can fail to conserve energy (Palubski et al. 2024; Fischer et al. 2024). However, most (sub)halos in our SIDM and WSIDM have a dimensionless scattering cross section  $\hat{\sigma} \equiv (\sigma/m_\chi)\rho_s r_s \lesssim 0.1$  (where  $\rho_s$  and  $r_s$  are the scale density and radius of the initial NFW profile; Mace et al. 2024), and are therefore in the long mean free path regime. Furthermore, our SIDM scattering algorithm has been calibrated against high-resolution controlled simulations (Yang & Yu 2022) and against halos with initial conditions drawn from the cosmological parent box used to initialize our zoom-in simulations (see Yang et al. 2023, Appendix B). Furthermore, we use a time-stepping parameter of  $\eta = 0.01$ , which is conservative for cosmological simulations. Thus, we expect discreteness noise to be the dominant systematic for our gravothermal evolution predictions, since we analyze (sub)halo density profiles down to 2000 particles, whereas

Palubski et al. (2024) and Mace et al. (2024) show that scatter can be inflated even at a resolution of  $\sim 10^5$  particles. It will therefore be important to critically assess the scatter in our (sub)halo density profiles predictions using higher-resolution simulations and semi-analytic models.

Finally, we discuss the impact of baryons. In the presence of baryons (e.g., the MW disk), the cored host density profiles in our SIDM and WSIDM simulations (Appendix E) will transform into cusps (e.g., Kaplinghat et al. 2014; Sameie et al. 2018; Robles et al. 2019; Rose et al. 2023; Correa et al. 2024), increasing the severity of tidal stripping and disruption. Thus, our SIDM and WSIDM SHMF suppression predictions in Figure 3 are likely underestimates. The presence of a central galaxy also enhances tidal stripping rates within a given DM model (Wang et al. 2024), which may further diversify the profiles of SIDM and WSIDM subhalos that orbit close to the host center. In particular, low-density subhalos in our SIDM and WSIDM runs (see Figures 8 and 9) may be disrupted by the disk, potentially bringing our central density predictions into better agreement with the data. Finally, baryons within (sub)halos may alter their density profiles via repeated episodes of supernova feedback (e.g., Pontzen & Governato 2012; Read et al. 2019). This effect is thought to be negligible for ultra-faint dwarfs, although it may alter the DM profiles of classical and bright dwarfs, which have masses  $10^9 \lesssim M_{\text{vir}}/M_\odot \lesssim 10^{11}$  (Tollet et al. 2016; Lazar et al. 2020). In the presence of self-interactions, the DM distribution responds efficiently to baryons, which changes the core-collapse timescale (e.g., Feng et al. 2021; Zhong et al. 2023; Yang 2024). Thus, it is timely to develop hydrodynamic simulations of SIDM and WSIDM (sub)halos that combine strong, velocity-dependent self-interactions and stellar feedback.

## 8. SUMMARY AND OUTLOOK

We have presented eight new cosmological zoom-in simulations of a MW analog, as the third installment of the COZMIC suite. We focused on the combined effects of  $P(k)$  suppression and DM self-interactions (Figure 1). For the first time, our simulations capture the full range of (sub)halos' gravothermal evolution, including core collapse. We found that  $P(k)$  suppression and self-interactions predicted in realistic SIDM particle models can simultaneously affect (sub)halo abundances and density profiles. Jointly modeling these effects will therefore be critical for probing WSIDM models with small-scale structure data.

Our main results are as follows:

1. (S)HMF suppression is determined by the suppression in the linear matter power spectrum  $P(k)$  used to generate initial conditions, rather than late-time self-interactions. The suppression is set by the kinetic decoupling temperature in our WSIDM model (Figure 3);
2. Power spectrum suppression reduces the SIDM core-collapse signature. This reduction is more severe when  $P(k)$  is more suppressed, and is more pronounced for isolated halos versus subhalos (Figures 4 and 6);

3. This reduction of the core-collapsed population is mainly due to (sub)halos' suppressed growth in WSIDM, which lowers their initial concentrations and increases their core-collapse timescales (Figure 7);
4. Subhalo density profiles are diversified by the strong, velocity-dependent interactions within the SIDM model we consider, but are not significantly affected when additionally introducing  $P(k)$  suppression, where the suppression is consistent with the current bounds from MW satellite abundance (Figure 8).
5. WSIDM models with sufficiently mild  $P(k)$  suppression can produce a significant anti-correlation between subhalo central density and pericentric distance due to core collapse in subhalos with small pericenters and core formation in low-density subhalos with large pericenters (Figure 9); these models also increase the abundance of extremely low-concentration isolated low-mass halos, relative to SIDM-only models.

These results highlight the importance of combining dwarf galaxy luminosity functions and density profile measurements to simultaneously constrain early and late-time DM physics. For example, WSIDM imply a possible new-physics discovery scenario, which is not available within SIDM models without  $P(k)$  suppression. In the WSIDM case,  $P(k)$  suppression is proportional to the SIDM coupling strength. Thus, models with stronger self-interactions produce more severe  $P(k)$  suppression, which partially or even entirely removes the core-collapse signature, as we show in this study. This degeneracy can be broken using observations that probe the (S)HMF, which provides an independent constraint on  $P(k)$  suppression. In other words, there is a finite range of WSIDM parameter space where a sizable fraction of dwarf galaxies both form *and* core collapse. Future efforts to map out this parameter space can complement previous studies that combine  $P(k)$  suppression and SIDM core formation (Vogelsberger et al. 2016; Drlica-Wagner et al. 2019).

In the context of dwarf galaxies, these results imply that both photometric surveys, which can probe dwarf galaxy abundances throughout the Local Volume, and spectroscopic facilities, which can probe the halo density profiles of faint systems, are critical for testing DM self-interaction physics (see Chakrabarti et al. 2022 for an overview of future observational facilities for studying DM). This synergy will be important as the Rubin Observatory Legacy Survey of Space

and Time (LSST; Ivezić et al. 2008) begins to discover large numbers of faint dwarf galaxies in the coming years (Mutlu-Pakdil et al. 2021; K. Tsiane et al., in preparation), increasing the precision of  $P(k)$  constraints (Nadler et al. 2024b). In parallel, combining dwarf galaxy data with independent observational probes of low-mass (sub)halos, including strong gravitational lensing and stellar stream perturbations, will enable powerful tests of DM self-interactions.

#### ACKNOWLEDGEMENTS

Halo catalogs, merger trees, and select particle snapshots will be made publicly available upon publication.

We thank Francis-Yan Cyr-Racine for helpful discussions. This work was supported by the John Templeton Foundation under grant ID #61884 and the U.S. Department of Energy under grant No. de-sc0008541 (D.Y. and H.-B.Y.). The opinions expressed in this publication are those of the authors and do not necessarily reflect the views of the John Templeton Foundation. V.G. acknowledges the support from NASA through the Astrophysics Theory Program, Award Number 21-ATP21-0135, the National Science Foundation (NSF) CAREER Grant No. PHY2239205, and from the Research Corporation for Science Advancement under the Cottrell Scholar Program. This research was supported in part by grant NSF PHY-2309135 to the Kavli Institute for Theoretical Physics (KITP).

The computations presented here were conducted through Carnegie's partnership in the Resnick High Performance Computing Center, a facility supported by Resnick Sustainability Institute at the California Institute of Technology. Computations were also performed using the computer clusters and data storage resources of the HPCC at UCR, which were funded by grants from NSF (MRI-2215705, MRI-1429826) and NIH (1S10OD016290-01A1). This work used data from the Milky Way-est suite of simulations, hosted at <https://web.stanford.edu/group/gfc/gfcsims/>, which was supported by the Kavli Institute for Particle Astrophysics and Cosmology at Stanford University, SLAC National Accelerator Laboratory, and the U.S. Department of Energy under contract number DE-AC02-76SF00515 to SLAC National Accelerator Laboratory.

*Software:* CONSISTENT-TREES (Behroozi et al. 2013b), HELPERS ([bitbucket.org/yymao/helpers/src/master/](https://bitbucket.org/yymao/helpers/src/master/)), JUPYTER ([jupyter.org](https://jupyter.org)), MATPLOTLIB (Hunter 2007), NUMPY (van der Walt et al. 2011), PYNBODY (Pontzen et al. 2013), ROCKSTAR (Behroozi et al. 2013a) SCIPY (Jones et al. 2001). SEABORN ([seaborn.pydata.org](https://seaborn.pydata.org))

#### REFERENCES

- Adhikari, S., Banerjee, A., Boddy, K. K., et al. 2022, [arXiv e-prints](https://arxiv.org/abs/2207.10638), arXiv:2207.10638
- An, R., Nadler, E. O., Benson, A., & Gluscevic, V. 2024, [arXiv e-prints](https://arxiv.org/abs/2411.03431), arXiv:2411.03431
- Ando, S., Horigome, S., Nadler, E. O., Yang, D., & Yu, H.-B. 2024, [arXiv e-prints](https://arxiv.org/abs/2403.16633), arXiv:2403.16633
- Andrade, K. E., Fuson, J., Gad-Nasr, S., et al. 2022, *MNRAS*, 510, 54

- Andrade, K. E., Kaplinghat, M., & Valli, M. 2024, *MNRAS*, 532, 4157
- Archidiacono, M., Bohr, S., Hannestad, S., Helboe Jørgensen, J., & Lesgourgues, J. 2017, *JCAP*, 2017, 010
- Atrio-Barandela, F. & Davidson, S. 1997, *PhRvD*, 55, 5886
- Atrio-Barandela, F. & Davidson, S. 2001, *PhRvD*, 64, 088301
- Balberg, S., Shapiro, S. L., & Inagaki, S. 2002, *ApJ*, 568, 475
- Behroozi, P. S., Wechsler, R. H., & Wu, H.-Y. 2013a, *ApJ*, 762, 109
- Behroozi, P. S., Wechsler, R. H., Wu, H.-Y., et al. 2013b, *ApJ*, 763, 18
- Bode, P., Ostriker, J. P., & Turok, N. 2001, *ApJ*, 556, 93
- Boehm, C., Fayet, P., & Schaeffer, R. 2001, *Phys. Lett. B*, 518, 8
- Böhm, C., Riazuelo, A., Hansen, S. H., & Schaeffer, R. 2002, *PhRvD*, 66, 083505
- Boehm, C. & Schaeffer, R. 2005, *A&A*, 438, 419
- Bond, J. R. & Szalay, A. S. 1983, *ApJ*, 274, 443
- Bryan, G. L. & Norman, M. L. 1998, *ApJ*, 495, 80
- Buch, D., Nadler, E. O., Wechsler, R. H., & Mao, Y.-Y. 2024, *ApJ*, 971, 79
- Buckley, M. R. & Peter, A. H. G. 2018, *PhR*, 761, 1
- Buckley, M. R., Zavala, J., Cyr-Racine, F.-Y., Sigurdson, K., & Vogelsberger, M. 2014, *PhRvD*, 90, 043524
- Cardona-Barrero, S., Battaglia, G., Nipoti, C., & Di Cintio, A. 2023, *MNRAS*, 522, 3058
- Carlesi, E., Sorce, J. G., Hoffman, Y., et al. 2016, *MNRAS*, 458, 900
- Chakrabarti, S., Drlica-Wagner, A., Li, T. S., et al. 2022, *arXiv e-prints*, arXiv:2203.06200
- Correa, C., Schaller, M., Schaye, J., et al. 2024, *arXiv e-prints*, arXiv:2403.09186
- Correa, C. A. 2021, *MNRAS*, 503, 920
- Cyr-Racine, F.-Y., Sigurdson, K., Zavala, J., et al. 2016, *PhRvD*, 93, 123527
- Despali, G., Heinze, F. M., Fassnacht, C. D., et al. 2024, *arXiv e-prints*, arXiv:2407.12910
- Drlica-Wagner, A., Mao, Y.-Y., Adhikari, S., et al. 2019, *arXiv e-prints*, arXiv:1902.01055
- Drlica-Wagner, A., Bechtol, K., Mau, S., et al. 2020, *ApJ*, 893, 47
- Ebisu, T., Ishiyama, T., & Hayashi, K. 2022, *PhRvD*, 105, 023016
- Egana-Ugrinovic, D., Essig, R., Gift, D., & LoVerde, M. 2021, *JCAP*, 2021, 013
- Errani, R., Navarro, J. F., Peñarrubia, J., Famaey, B., & Ibata, R. 2023, *MNRAS*, 519, 384
- Essig, R., McDermott, S. D., Yu, H.-B., & Zhong, Y.-M. 2019, *PhRvL*, 123, 121102
- Feng, J. L., Kaplinghat, M., Tu, H., & Yu, H.-B. 2009, *JCAP*, 2009, 004
- Feng, J. L., Kaplinghat, M., & Yu, H.-B. 2010, *PhRvL*, 104, 151301
- Feng, J. L., Tu, H., & Yu, H.-B. 2008, *JCAP*, 2008, 043
- Feng, W.-X., Yu, H.-B., & Zhong, Y.-M. 2021, *ApJL*, 914, L26
- Fischer, M. S., Dolag, K., & Yu, H.-B. 2024, *A&A*, 689, A300
- Garani, R., Redi, M., & Tesi, A. 2022, *JCAP*, 2022, 012
- Gilman, D., Bovy, J., Treu, T., et al. 2021, *MNRAS*, 507, 2432
- Gilman, D., Zhong, Y.-M., & Bovy, J. 2023, *PhRvD*, 107, 103008
- Gluscevic, V., Ali-Haimoud, Y., Bechtol, K., et al. 2019, *BAAS*, 51, 134
- Hahn, O. & Abel, T. 2011, *MNRAS*, 415, 2101
- Hannestad, S. & Scherrer, R. J. 2000, *PhRvD*, 62, 043522
- Hinshaw, G., Larson, D., Komatsu, E., et al. 2013, *ApJS*, 208, 19
- Hunter, J. D. 2007, *Computing in Science Engineering*, 9, 90
- Huo, R. 2020, *Physics Letters B*, 802, 135251
- Huo, R., Kaplinghat, M., Pan, Z., & Yu, H.-B. 2018, *Physics Letters B*, 783, 76
- Iršič, V., Viel, M., Haehnelt, M. G., et al. 2017, *PhRvD*, 96, 023522
- Iršič, V., Viel, M., Haehnelt, M. G., et al. 2024, *PhRvD*, 109, 043511
- Ivezić, Ž., Kahn, S. M., Tyson, J. A., et al. 2008, *ApJ*, 873, 111
- Jones, E., Oliphant, T., Peterson, P., et al. 2001, *SciPy: Open source scientific tools for Python*, [Online; [scipy.org](http://scipy.org)]
- Kahlhoefer, F., Kaplinghat, M., Slatyer, T. R., & Wu, C.-L. 2019, *JCAP*, 2019, 010
- Kaplinghat, M., Keeley, R. E., Linden, T., & Yu, H.-B. 2014, *PhRvL*, 113, 021302
- Kaplinghat, M., Tulin, S., & Yu, H.-B. 2016, *PhRvL*, 116, 041302
- Kaplinghat, M., Valli, M., & Yu, H.-B. 2019, *MNRAS*, 490, 231
- Kim, S. Y. & Peter, A. H. G. 2021, *arXiv e-prints*, arXiv:2106.09050
- Koda, J. & Shapiro, P. R. 2011, *MNRAS*, 415, 1125
- Kong, D., Kaplinghat, M., Yu, H.-B., Fraternali, F., & Mancera Piña, P. E. 2022, *ApJ*, 936, 166
- Kong, D., Yang, D., & Yu, H.-B. 2024, *ApJL*, 965, L19
- Lazar, A., Bullock, J. S., Boylan-Kolchin, M., et al. 2020, *MNRAS*, 497, 2393
- Lesgourgues, J. 2011, *arXiv e-prints*, arXiv:1104.2932
- Lewis, A. & Bridle, S. 2002, *PhRvD*, 66, 103511
- Lovell, M. R. & Zavala, J. 2023, *MNRAS*, 520, 1567
- Ludlow, A. D., Schaye, J., & Bower, R. 2019, *MNRAS*, 488, 3663
- Mace, C., Carton Zeng, Z., Peter, A. H. G., et al. 2024, *arXiv e-prints*, arXiv:2402.01604
- Mancera Piña, P. E., Fraternali, F., Oosterloo, T., et al. 2022, *MNRAS*, 512, 3230
- Mancera Piña, P. E., Fraternali, F., Adams, E. A. K., et al. 2019, *ApJL*, 883, L33
- Mancera Piña, P. E., Fraternali, F., Oman, K. A., et al. 2020, *MNRAS*, 495, 3636
- Mansfield, P., Darragh-Ford, E., Wang, Y., et al. 2024, *ApJ*, 970, 178
- McAlpine, S., Helly, J. C., Schaller, M., et al. 2022, *MNRAS*, 512, 5823

- Meshveliani, T., Lovell, M. R., Crain, R. A., & Pfeffer, J. 2024, *MNRAS*, 532, 1296
- Minor, Q., Gad-Nasr, S., Kaplinghat, M., & Vegetti, S. 2021a, *MNRAS*, 507, 1662
- Minor, Q., Kaplinghat, M., Chan, T. H., & Simon, E. 2021b, *MNRAS*, 507, 1202
- Mutlu-Pakdil, B., Sand, D. J., Crnojević, D., et al. 2021, *ApJ*, 918, 88
- Nadler, E. O., An, R., Gluscevic, V., Benson, A., & Du, X. 2024a, *arXiv e-prints*, [arXiv:2410.03635](https://arxiv.org/abs/2410.03635)
- Nadler, E. O., Banerjee, A., Adhikari, S., Mao, Y.-Y., & Wechsler, R. H. 2020a, *ApJ*, 896, 112
- Nadler, E. O., Birrer, S., Gilman, D., et al. 2021a, *ApJ*, 917, 7
- Nadler, E. O., Gluscevic, V., Boddy, K. K., & Wechsler, R. H. 2019a, *ApJL*, 878, L32
- Nadler, E. O., Gluscevic, V., Driskell, T., et al. 2024b, *ApJ*, 967, 61
- Nadler, E. O., Mao, Y.-Y., Green, G. M., & Wechsler, R. H. 2019b, *ApJ*, 873, 34
- Nadler, E. O., Yang, D., & Yu, H.-B. 2023a, *ApJL*, 958, L39
- Nadler, E. O., Wechsler, R. H., Bechtol, K., et al. 2020b, *ApJ*, 893, 48
- Nadler, E. O., Drlica-Wagner, A., Bechtol, K., et al. 2021b, *PhRvL*, 126, 091101
- Nadler, E. O., Mansfield, P., Wang, Y., et al. 2023b, *ApJ*, 945, 159
- Navarro, J. F., Frenk, C. S., & White, S. D. M. 1997, *ApJ*, 490, 493
- Nishikawa, H., Boddy, K. K., & Kaplinghat, M. 2020, *PhRvD*, 101, 063009
- Pace, A. B., Erkal, D., & Li, T. S. 2022, *ApJ*, 940, 136
- Palubski, I., Slone, O., Kaplinghat, M., Lisanti, M., & Jiang, F. 2024, *arXiv e-prints*, [arXiv:2402.12452](https://arxiv.org/abs/2402.12452)
- Pontzen, A. & Governato, F. 2012, *MNRAS*, 421, 3464
- Pontzen, A., Roškar, R., Stinson, G., & Woods, R. 2013, pynbody: N-Body/SPH analysis for python, Astrophysics Source Code Library, record ascl:1305.002
- Read, J. I., Walker, M. G., & Steger, P. 2018, *MNRAS*, 481, 860
- Read, J. I., Walker, M. G., & Steger, P. 2019, *MNRAS*, 484, 1401
- Roberts, M. G., Kaplinghat, M., Valli, M., & Yu, H.-B. 2024, *arXiv e-prints*, [arXiv:2407.15005](https://arxiv.org/abs/2407.15005)
- Robles, V. H., Kelley, T., Bullock, J. S., & Kaplinghat, M. 2019, *MNRAS*, 490, 2117
- Rocha, M., Peter, A. H. G., Bullock, J. S., et al. 2013, *MNRAS*, 430, 81
- Rose, J. C., Torrey, P., Vogelsberger, M., & O’Neil, S. 2023, *MNRAS*, 519, 5623
- Sagunski, L., Gad-Nasr, S., Colquhoun, B., Robertson, A., & Tulin, S. 2021, *JCAP*, 2021, 024
- Sameie, O., Benson, A. J., Sales, L. V., et al. 2019, *ApJ*, 874, 101
- Sameie, O., Creasey, P., Yu, H.-B., et al. 2018, *MNRAS*, 479, 359
- Sameie, O., Yu, H.-B., Sales, L. V., Vogelsberger, M., & Zavala, J. 2020, *PhRvL*, 124, 141102
- Silverman, M., Bullock, J. S., Kaplinghat, M., Robles, V. H., & Valli, M. 2023, *MNRAS*, 518, 2418
- Slone, O., Jiang, F., Lisanti, M., & Kaplinghat, M. 2023, *PhRvD*, 107, 043014
- Spergel, D. N. & Steinhardt, P. J. 2000, *PhRvL*, 84, 3760
- Springel, V. 2005, *MNRAS*, 364, 1105
- Tollet, E., Macciò, A. V., Dutton, A. A., et al. 2016, *MNRAS*, 456, 3542
- Tran, V., Gilman, D., Vogelsberger, M., et al. 2024, *PhRvD*, 110, 043048
- Tulin, S. & Yu, H.-B. 2018, *PhR*, 730, 1
- Tulin, S., Yu, H.-B., & Zurek, K. M. 2013, *PhRvD*, 87, 115007
- Turner, H. C., Lovell, M. R., Zavala, J., & Vogelsberger, M. 2021, *MNRAS*, 505, 5327
- Valli, M. & Yu, H.-B. 2018, *Nature Astronomy*, 2, 907
- van den Aarssen, L. G., Bringmann, T., & Pfrommer, C. 2012, *PhRvL*, 109, 231301
- van der Walt, S., Colbert, S. C., & Varoquaux, G. 2011, *Computing in Science Engineering*, 13, 22
- Viel, M., Becker, G. D., Bolton, J. S., & Haehnelt, M. G. 2013, *PhRvD*, 88, 043502
- Vogelsberger, M., Zavala, J., Cyr-Racine, F.-Y., et al. 2016, *MNRAS*, 460, 1399
- Vogelsberger, M., Zavala, J., & Loeb, A. 2012, *MNRAS*, 423, 3740
- Wang, Y., Mansfield, P., Nadler, E. O., et al. 2024, *arXiv e-prints*, [arXiv:2408.01487](https://arxiv.org/abs/2408.01487)
- Wempe, E., Lavaux, G., White, S. D. M., et al. 2024, *A&A*, 691, A348
- Yang, D. 2024, *PhRvD*, 110, 103044
- Yang, D., Nadler, E. O., & Yu, H.-B. 2023, *ApJ*, 949, 67
- Yang, D., Nadler, E. O., & Yu, H.-B. 2024a, *arXiv e-prints*, [arXiv:2406.10753](https://arxiv.org/abs/2406.10753)
- Yang, D., Nadler, E. O., Yu, H.-B., & Zhong, Y.-M. 2024b, *JCAP*, 2024, 032
- Yang, D. & Yu, H.-B. 2021, *PhRvD*, 104, 103031
- Yang, D. & Yu, H.-B. 2022, *JCAP*, 2022, 077
- Yunis, R., Argüelles, C. R., & López Nacir, D. 2020, *JCAP*, 2020, 041
- Yunis, R., Argüelles, C. R., Scóccola, C. G., López Nacir, D., & Giordano, G. 2022, *JCAP*, 2022, 024
- Zavala, J., Lovell, M. R., Vogelsberger, M., & Burger, J. D. 2019, *PhRvD*, 100, 063007
- Zeng, Z. C., Peter, A. H. G., Du, X., et al. 2022, *MNRAS*, 513, 4845
- Zeng, Z. C., Peter, A. H. G., Du, X., et al. 2023, *arXiv e-prints*, [arXiv:2310.09910](https://arxiv.org/abs/2310.09910)
- Zhang, X., Yu, H.-B., Yang, D., & An, H. 2024a, *ApJL*, 968, L13
- Zhang, X., Yu, H.-B., Yang, D., & Nadler, E. O. 2024b, *arXiv e-prints*, [arXiv:2409.19493](https://arxiv.org/abs/2409.19493)
- Zhong, Y.-M., Yang, D., & Yu, H.-B. 2023, *MNRAS*, 526, 758

## APPENDIX

## A. CONVERGENCE TESTS

To assess convergence, we resimulate all models using four MUSIC refinement regions, yielding a high-resolution DM particle mass of  $4 \times 10^5 M_\odot$ ; we use a softening of  $\epsilon = 170 \text{ pc } h^{-1}$  for these “low-resolution” (LR) runs. Note that our LR runs have equivalent resolution to the “fiducial” simulations in Paper I, while our fiducial-resolution simulations have equivalent resolution to the “high-resolution” runs in Paper I. Below, we compare our LR and fiducial-resolution simulations to analyze (S)HMF (Appendix A.1) and  $R_{\text{max}}-V_{\text{max}}$  relation (Appendix A.2) convergence.

## A.1. Mass Functions

In Paper I, we showed that SHMF suppression is converged across zoom-in hosts and beyond-CDM models for simulations with identical settings to ours. Here, we repeat this analysis for a single host, because we only simulate one MW-like system in this work, and we focus on our SIDM and WSIDM results because convergence of SHMF suppression due to  $P(k)$  suppression alone was already demonstrated in Paper I.

Figure 10 shows the isolated halo (left) and subhalo (right) peak mass function in our LR and fiducial-resolution simulations. We impose a present-day virial mass cut corresponding to 300 LR particles and 2400 fiducial-resolution particles, i.e.,  $M_{\text{vir}} > 1.2 \times 10^8 M_\odot$ . Isolated halo mass functions are converged at the percent level above this threshold. Subhalo abundances are less well converged, but still only deviate from the fiducial-resolution result by at most  $\approx 10\%$ ; at high subhalo masses, Poisson uncertainties are large and we sometimes observe enhancements in LR subhalo abundances. Thus, our fiducial-resolution simulations resolve the isolated halo and SHMF well for  $M_{\text{vir}} > 1.2 \times 10^8 M_\odot$ , which is the cut we impose in our main analyses related to subhalo profiles. Convergence down to the 300-particle limit in our fiducial-resolution simulations, i.e.,  $M_{\text{vir}} > 1.5 \times 10^7 M_\odot$ , will need to be tested using even higher-resolution simulations in future work. However, none of our main conclusions rely on (sub)halos in this regime.

A.2.  $R_{\text{max}}-V_{\text{max}}$  Relations

To assess convergence of  $R_{\text{max}}$  and  $V_{\text{max}}$ , Figure 11 shows  $R_{\text{max}}$  (left) and  $V_{\text{max}}$  (right) distributions for isolated halos. We impose a mass cut corresponding to 2000 LR particles and 16000 fiducial-resolution particles, i.e.,  $M_{\text{vir}} > 8 \times 10^8 M_\odot$ ; this yields too few subhalos to measure the distributions reliably, so we focus on isolated halos. All pairs of LR and fiducial-resolution distributions are statistically consistent: two-sample Kolmogorov–Smirnov (KS) tests yield  $p \gg 0.05$  in all cases. The  $V_{\text{max}}$  distributions are extremely similar, with  $p > 0.99$  from all two-sample KS tests, while KS tests yield  $p \approx 0.3$  for all  $R_{\text{max}}$  distribution comparisons.

Thus, our fiducial-resolution simulations resolve isolated halo  $R_{\text{max}}$  and  $V_{\text{max}}$  distributions well for  $M_{\text{vir}} > 8 \times 10^8 M_\odot$ . A larger simulation suite is needed to statistically assess convergence for subhalos, and higher-resolution runs are needed to assess convergence in the  $M_{\text{vir}} < 8 \times 10^8 M_\odot$  regime. Nonetheless, by inspecting  $R_{\text{max}}$  and  $V_{\text{max}}$  evolution histories for individual pairs of (sub)halos matched between our LR and fiducial-resolution runs, we do not find evidence that our results are biased in this regime.

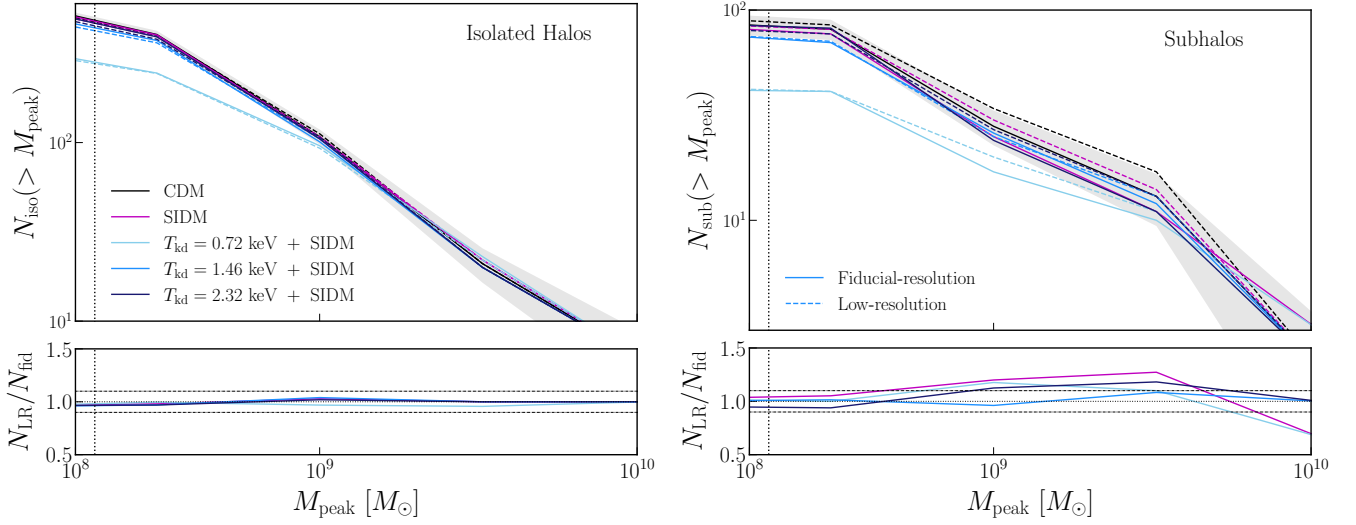
## B. COMPARISON TO WDM (SUB)HALO MASS FUNCTION SUPPRESSION

Figure 12 compares isolated halo and SHMFs in our fiducial-resolution  $T_{\text{kd}}$ -only and half mode-matched WDM simulations, using our usual  $M_{\text{vir}} > 1.5 \times 10^7 M_\odot$  cut in all cases. The  $T_{\text{kd}}$ -only mass functions are less suppressed than the half mode-matched WDM results. This is similar to our comparison between DM–baryon scattering and WDM models in Paper I, where we showed that the reduction in SHMF suppression for interacting DM models is largely due to the difference in the shape of the initial  $P(k)$  cutoff rather than DAOs. Thus, we expect the low-amplitude DAOs in our  $T_{\text{kd}}$  models to have a small impact on (sub)halo abundances given our  $M_{\text{vir}}$  cut, although we note that the difference between our  $T_{\text{kd}}$ -only and half mode-matched WDM mass functions is largest for our  $T_{\text{kd}} = 0.72 \text{ keV}$ -only run, which has a DAO that is fully resolved in our simulations when mapping wave numbers to masses in linear theory (see the right panel of Figure 1).

The bottom panels of Figure 12 show mass function ratios relative to CDM for our  $T_{\text{kd}}$ -only and half mode-matched WDM simulations; we also show results for the “effective” WDM models used to assess the impact of low-mass (sub)halo erasure on gravothermal evolution in Section 5. We derive these “effective” WDM models following the procedure for DM–baryon scattering simulations in Paper I. In particular, we apply the best-fit WDM SHMF suppression model derived in Paper I to our CDM simulations, and we find the “effective” WDM mass,  $m_{\text{WDM,eff}}$ , that matches the total number of isolated halos (or subhalos) with  $M_{\text{vir}} > 1.5 \times 10^7 M_\odot$  in each of our  $T_{\text{kd}}$ -only simulations. Thus, the “effective” WDM curves in the bottom panels of Figure 12 closely match the  $T_{\text{kd}}$ -only results at  $M_{\text{peak}} = 1.5 \times 10^7 M_\odot$  by construction, and the differences in the shape of the suppression at higher (sub)halo masses reflect differences in the underlying shapes of  $P(k)$ .

## C. MATCHED SUBHALO EVOLUTION

Figures 13 and 14 respectively show the evolution of matched subhalos in our  $T_{\text{kd}} = 0.72$  and  $2.32 \text{ keV}$  simulations with and without self-interactions, in the same format as Figure 7.



**Figure 10.** Same as Figure 3, but comparing our fiducial-resolution (solid) and low-resolution (dashed) simulations to assess convergence. Both resolution levels are subject to a  $M_{\text{vir}} > 1.2 \times 10^8 M_{\odot}$  cut, corresponding to 300 particles in the low-resolution simulations and 2400 particles in the fiducial-resolution simulations. The vertical dotted line shows the 300-particle limit for the low-resolution simulations. The horizontal dotted–dashed lines in the bottom panels show  $\pm 10\%$  deviations from the fiducial-resolution result.

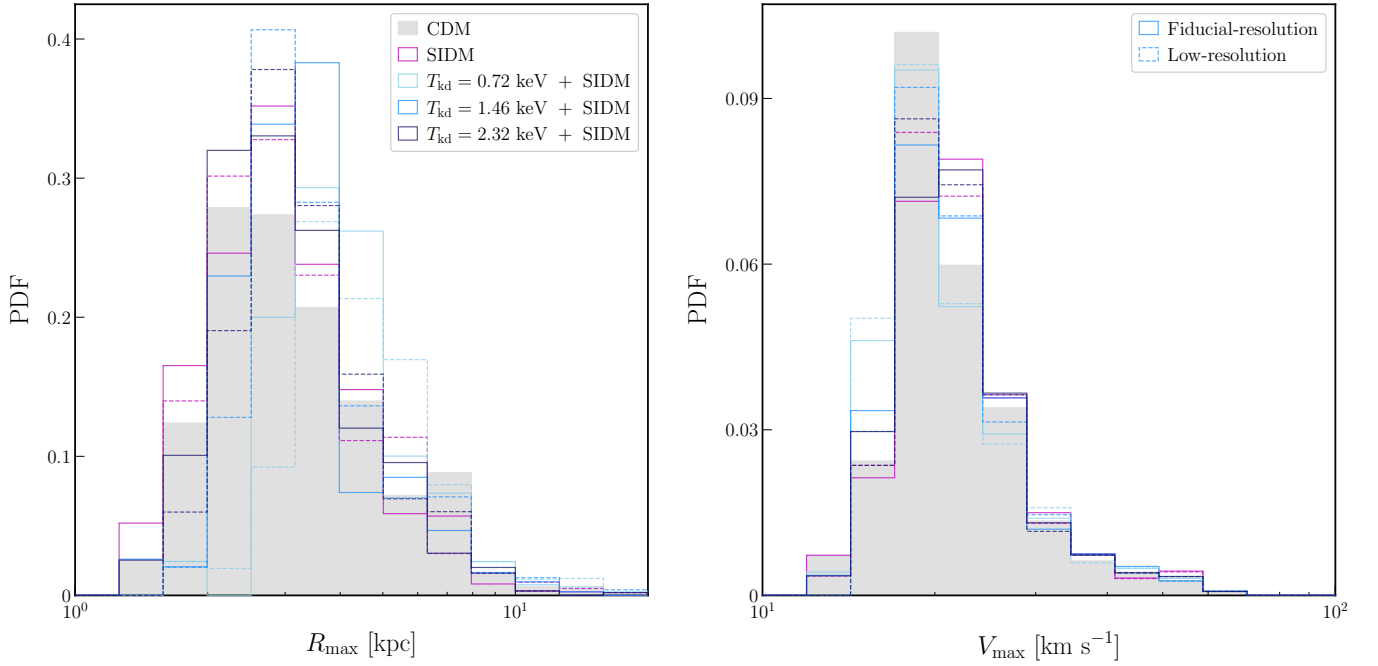


**Figure 11.** Normalized distributions of  $R_{\text{max}}$  (left) and  $V_{\text{max}}$  (right) for isolated halos with  $M_{\text{vir}} > 8 \times 10^8 M_{\odot}$  in our CDM (black), SIDM (magenta), and  $T_{\text{kd}} = 0.72, 1.46,$  and  $2.32$  keV WSIDM simulations (light to dark blue). Solid (dashed) lines show the fiducial-resolution (low-resolution) result.

For the  $T_{\text{kd}} = 0.72$  keV case, only the high-mass subhalo (top row) matches the system shown in Figure 7; we cannot identify the medium and low-mass systems shown in the middle and bottom rows of Figure 7 because they do not form in the  $T_{\text{kd}} = 0.72$  keV runs. Instead, the middle and bottom rows of Figure 13 show subhalos with values of  $V_{\text{peak,CDM}}$  compa-

rable to the medium and low-mass systems in Figure 7. We draw the following conclusions from Figure 13:

- The high-mass subhalo (top row) has a significantly suppressed growth history relative to its  $T_{\text{kd}} = 1.46$  keV counterpart in Figure 7. This difference is particularly noticeable at late times, and tidal stripping of the

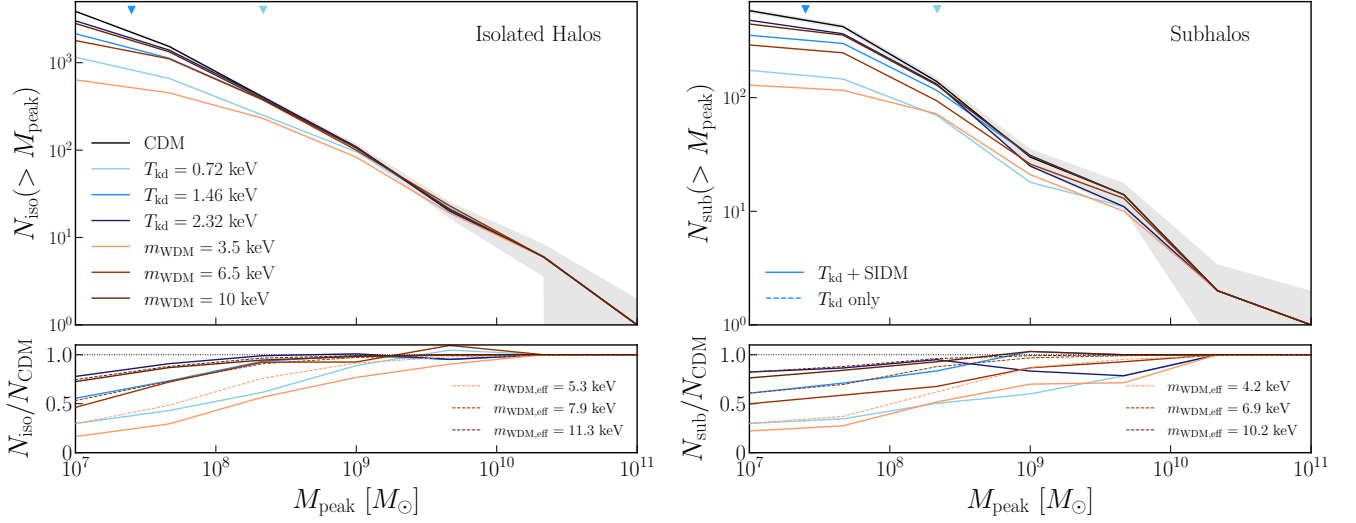


**Figure 12.** Same as Figure 3, but comparing our  $T_{\text{kd}} = 0.72, 1.46,$  and  $2.32$  keV-only isolated halo (left) and subhalo (right) mass functions (light to dark blue) to our  $m_{\text{WDM}} = 3.5, 6.5,$  and  $10$  keV simulations (light to dark red). Dashed lines in the bottom panels show “effective” WDM models matched to each of our  $T_{\text{kd}}$ -only runs.

$T_{\text{kd}} = 0.72$  keV subhalo is enhanced near pericenter relative to the CDM and SIDM versions of the subhalo, regardless of whether self-interactions are included.

- The moderate-mass subhalo (middle row) is mildly core-collapsed in our SIDM simulation, and its accelerated gravothermal evolution appears to follow an early major merger. This subhalo’s growth is severely suppressed (and mildly delayed) in the  $T_{\text{kd}} = 0.72$  keV runs; its present-day  $V_{\text{max}}$  is slightly enhanced in the WSIDM simulation compared to the  $T_{\text{kd}} = 0.72$  keV-only case, but the difference is minor.
- The low-mass subhalo (bottom row) is again mildly core-collapsed in our SIDM simulation, while its growth is extremely suppressed and delayed in the  $T_{\text{kd}} = 0.72$  keV runs. In addition, its orbital phase shifts after first pericenter in these runs, relative to the CDM and SIDM versions of the system, which is likely driven by differences in the subhalo’s density profile. In Appendix E, we show that the host density profile has a similar core in our SIDM and WSIDM simulations and a similar cusp in our CDM and  $T_{\text{kd}}$ -only simulations; thus, the orbital phase shift cannot be due to differences in the host potential, since the phase is similar in our CDM and SIDM simulations and in our  $T_{\text{kd}} = 0.72$  keV-only and WSIDM simulations.

For the  $T_{\text{kd}} = 2.32$  keV case, we recover all three systems shown in Figure 7, and plot them in the corresponding rows of Figure 14. We draw the following conclusions from Figure 14:

- The high-mass subhalo (top row) behaves very similarly to the  $T_{\text{kd}} = 1.46$  keV case shown in Figure 7; in the  $T_{\text{kd}} = 2.32$  keV WSIDM run, its present-day

$V_{\text{max}}$  is slightly *enhanced* relative to SIDM and to the  $T_{\text{kd}} = 1.46$  keV simulation, but the difference is small.

- The moderate-mass subhalo (middle row) has its gravothermal evolution *accelerated* in the  $T_{\text{kd}} = 2.32$  keV WSIDM simulation, relative to both SIDM and the  $T_{\text{kd}} = 1.46$  keV case.
- The low-mass subhalo (bottom row) reaches a present-day  $V_{\text{max}}$  slightly *above* CDM in the  $T_{\text{kd}} = 2.32$  keV WSIDM simulation, in contrast to its slightly suppressed  $V_{\text{max}}$  in the  $T_{\text{kd}} = 1.46$  keV WSIDM case.

Intriguingly, all three examples of  $T_{\text{kd}} = 2.32$  keV WSIDM subhalos have slightly *enhanced*  $V_{\text{max}}$  histories relative to both SIDM and our more extreme WSIDM simulations. This contrasts our result in Figure 6, where the predicted  $\tau_0$  distributions of  $T_{\text{kd}} = 2.32$  keV WSIDM (sub)halos were systematically shifted to lower  $\tau_0$  compared to SIDM. However, the  $\tau_0$  prediction is based on applying the parametric model to the  $T_{\text{kd}} = 2.32$  keV-only simulation, and it is possible that nonlinear effects that are not captured by the parametric model affect (sub)halos’ gravothermal evolution in our  $T_{\text{kd}} = 2.32$  keV WSIDM simulation. We leave a detailed exploration of these results to future study.

## D. DWARF GALAXY SUBHALOS

### D.1. Subhalo Density Profiles

Figure 15 shows subhalo density profiles in our  $T_{\text{kd}} = 0.72$  and  $2.32$  keV WSIDM simulations, analogous to Figure 8; see Section 6.1 for a discussion of these results.

### D.2. Central Density–Pericenter Relation

Figure 16 shows subhalo central density–pericenter relations for our  $T_{\text{kd}} = 0.72$  and  $2.32$  keV simulations with and without self-interactions; see Section 6.2 for a discussion of these results.

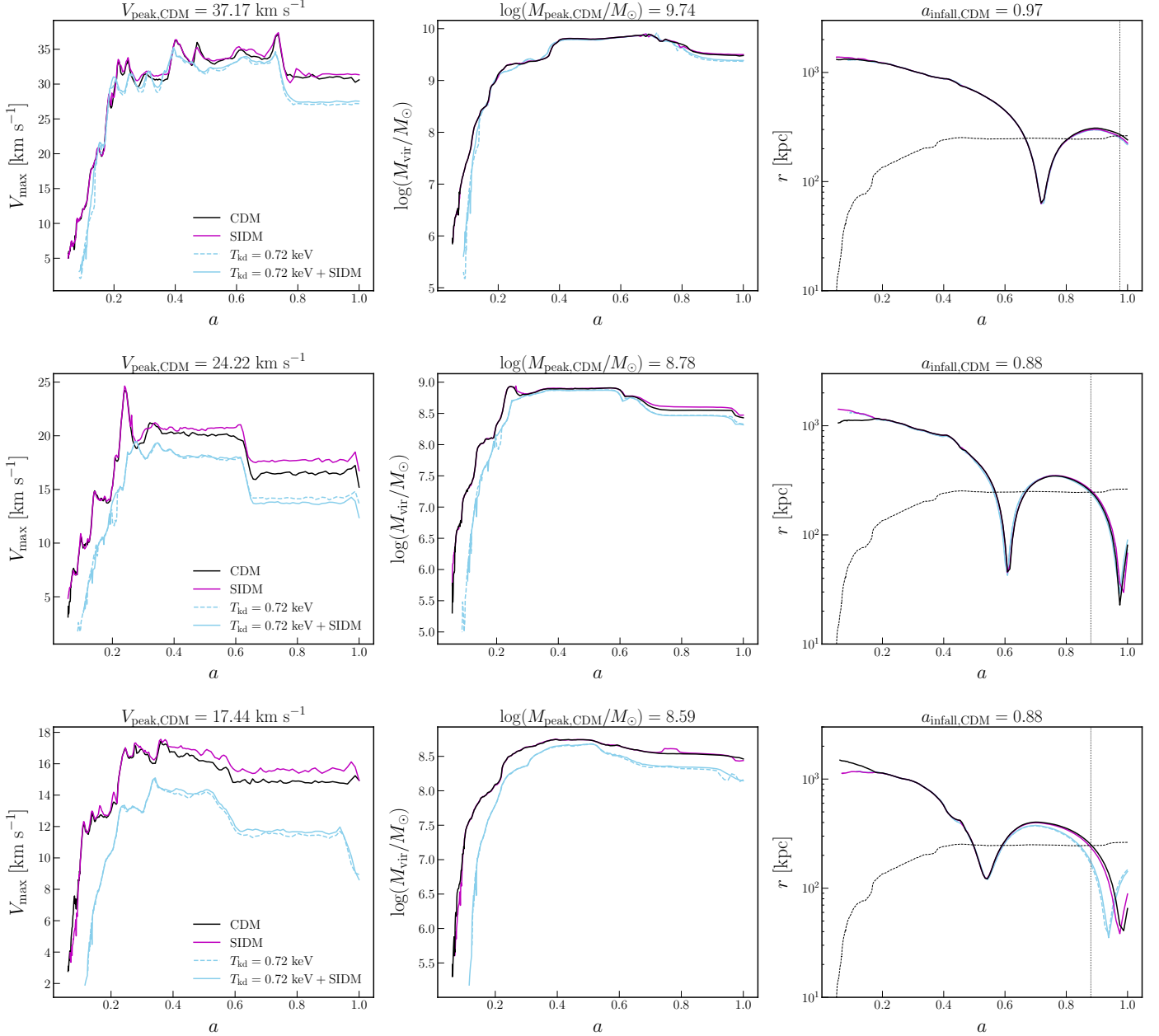


**Figure 13.** Same as Figure 7, for matched subhalos in our  $T_{\text{kd}} = 0.72 \text{ keV}$  simulations. The high-mass subhalo (top row) is the same as that in Figure 7, while the medium-mass (middle row) and low-mass (bottom row) subhalos are different systems than those shown in the corresponding rows of Figure 7.

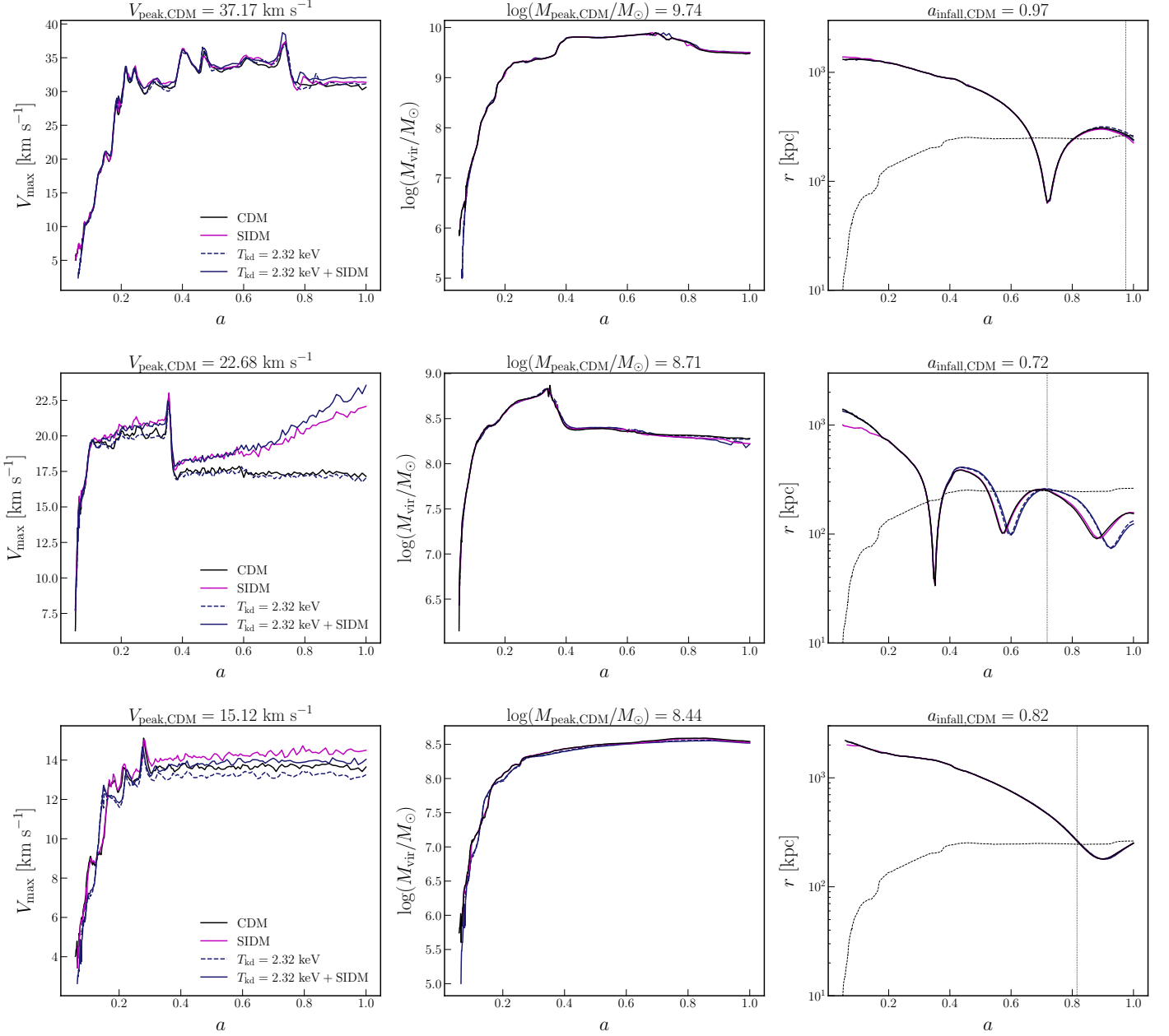
### E. HOST HALO DENSITY PROFILES

Figure 17 shows the density profile of the MW-like host halo in our CDM, SIDM, WSIDM, and  $T_{\text{kd}}$ -only simulations. The host has a prominent kiloparsec-scale density core in WSIDM simulations, independent of the  $T_{\text{kd}}$  model and consistent with the core in our SIDM simulation. Note that the SIDM host’s core size is similar to that found in Yang et al. (2023). Meanwhile, in our  $T_{\text{kd}}$ -only simulations, the host’s density profile is not significantly altered relative to CDM. This is expected because  $P(k)$  suppression is negligible on

the scale of the host in our  $T_{\text{kd}}$  models (see the right panel of Figure 1), and the host halo mass accretion history is nearly identical in all cases.

As discussed in Section 7.3, we expect these differences between SIDM and CDM (or WSIDM and  $T_{\text{kd}}$ -only) density profiles to be erased in the presence of baryons (Kaplinghat et al. 2014; Sameie et al. 2018; Robles et al. 2019; Rose et al. 2023; Correa et al. 2024).





**Figure 14.** Same as Figure 7, for matched subhalos in our  $T_{\text{kd}} = 2.32$  keV simulations. Each row shows the same system as the corresponding row in Figure 7.

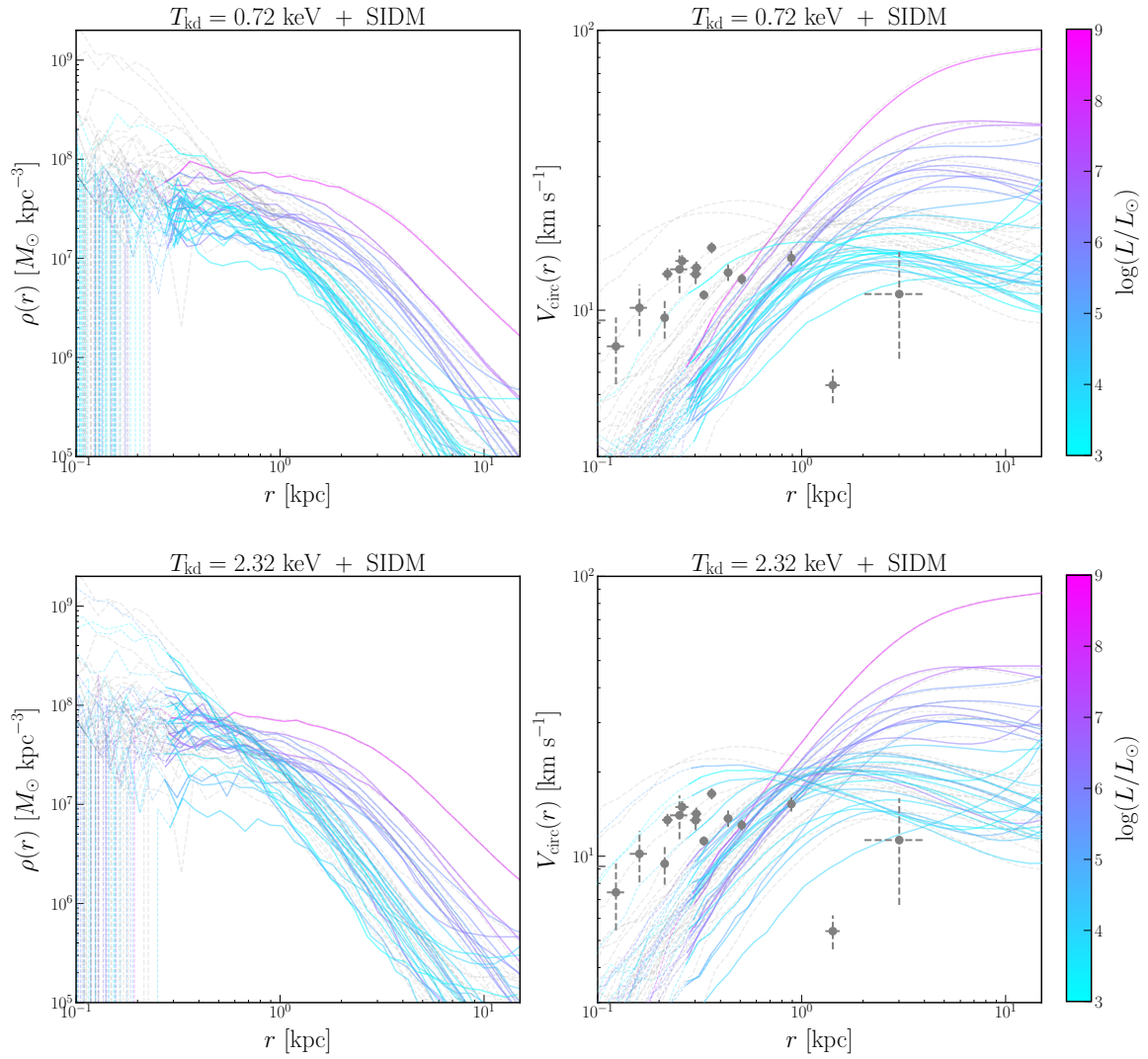


**Figure 15.** Same as Figure 8, for our  $T_{\text{kd}} = 0.72$  (top) and 2.32 keV (bottom) WSIDM simulations. Faint gray lines in both rows show the SIDM result.

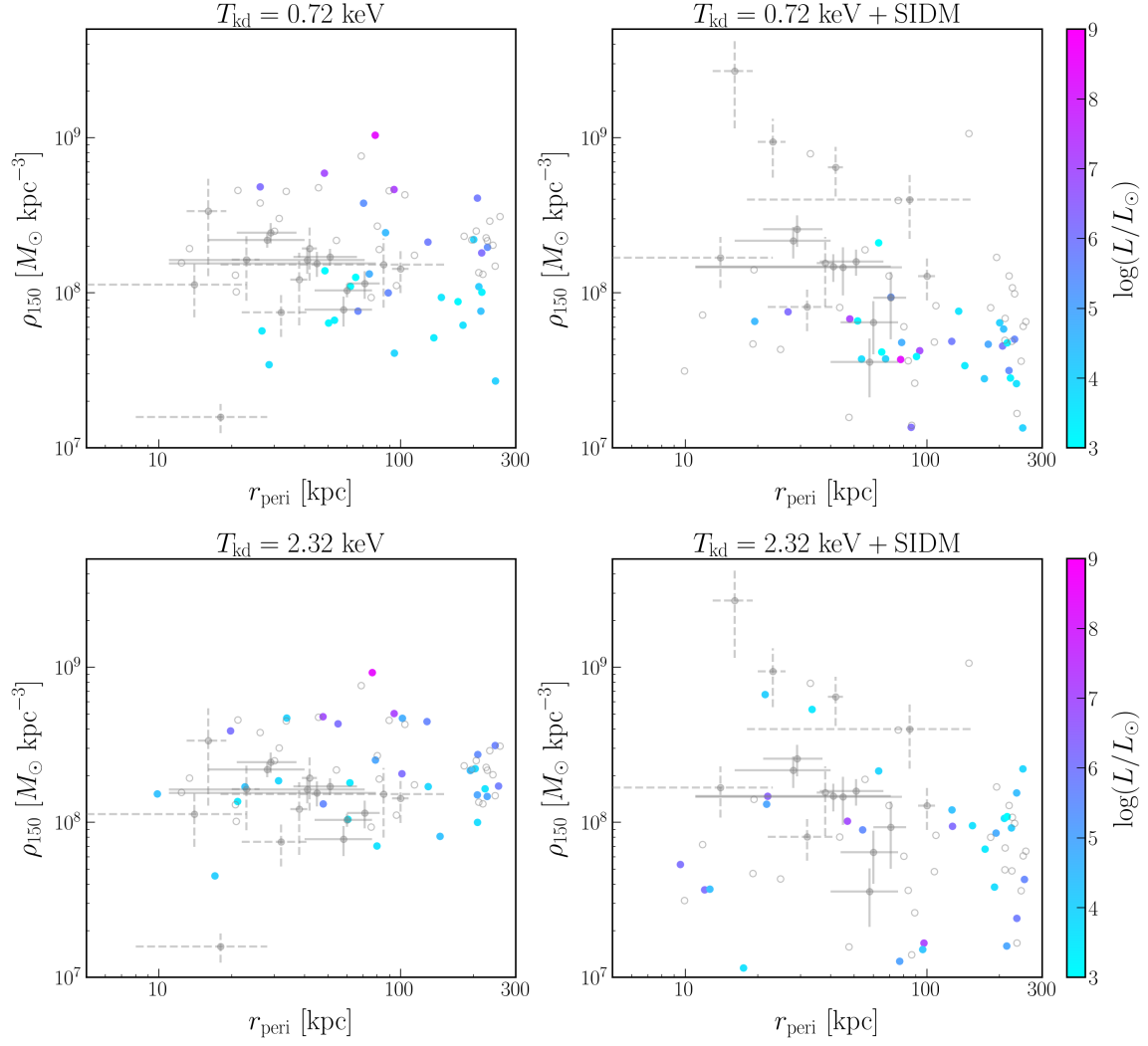


**Figure 16.** Same as Figure 9, for our  $T_{\text{kd}} = 0.72$  keV-only (top left),  $T_{\text{kd}} = 0.72$  keV WSIDM (top right),  $T_{\text{kd}} = 2.32$  keV-only (bottom left), and  $T_{\text{kd}} = 2.32$  keV WSIDM (bottom right) simulations. In the top left panel, open gray circles show the CDM result; in all other panels, they show the SIDM result.

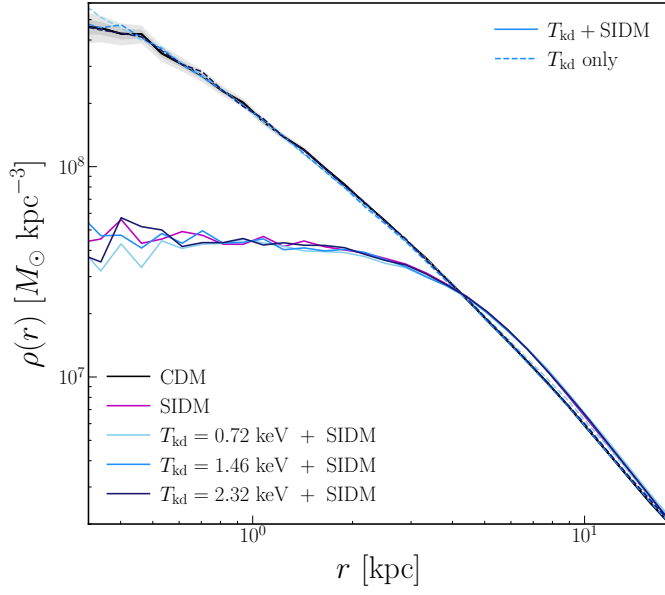


**Figure 17.** Density profile of our MW-like host halo in CDM (black), SIDM (magenta), and WSIDM models with  $T_{\text{kd}} = 0.72$ , 1.46, and 2.32 keV (lightest to darkest blue). Corresponding  $T_{\text{kd}}$ -only simulations are shown by dashed lines. Dark (light) gray bands show  $1\sigma$  ( $2\sigma$ ) Poisson uncertainties on the CDM measurement. The minimum radius shown,  $2.8\epsilon = 320$  pc corresponds to the convergence radius of our simulations. For  $r \gtrsim 20$  kpc, the profiles remain identical out to the virial radius.